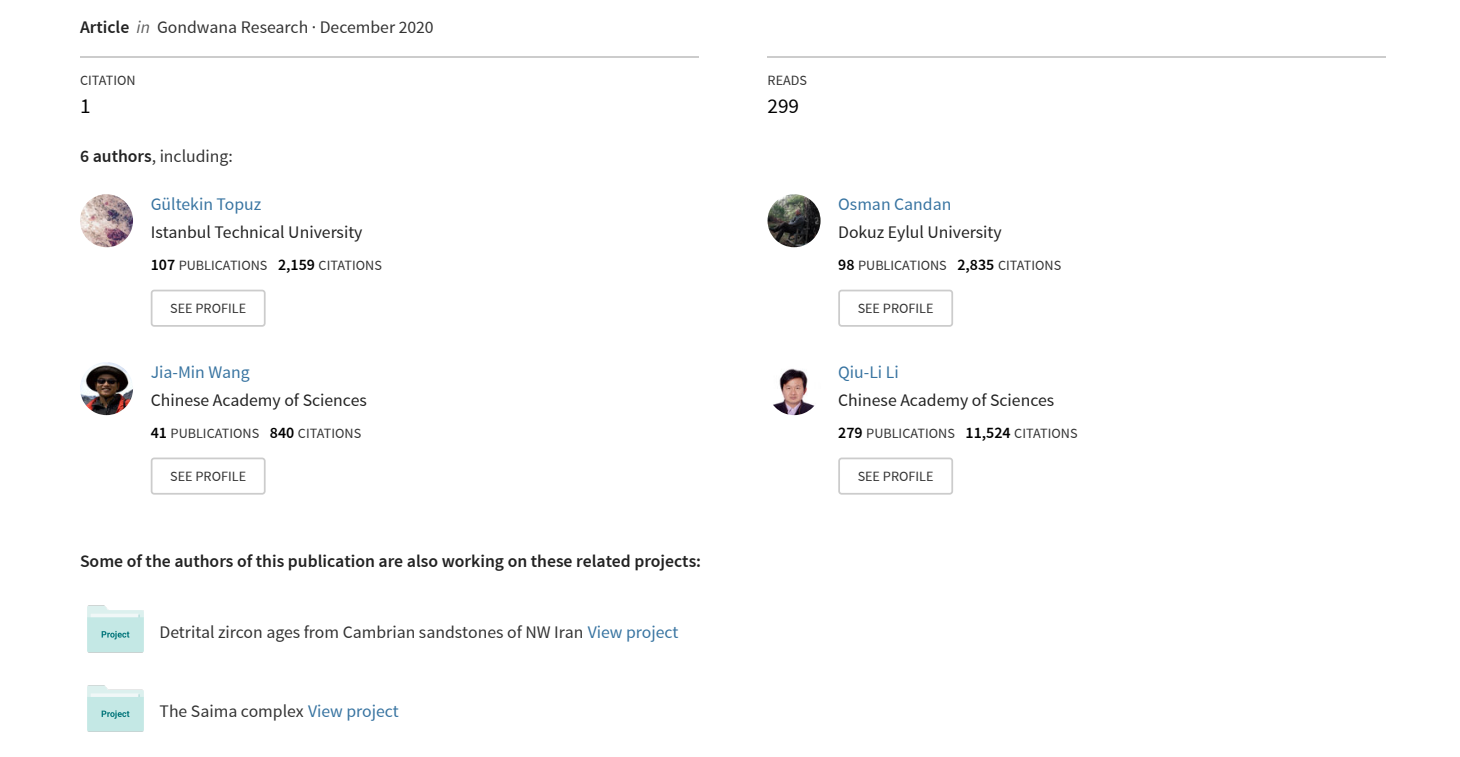
Silurian A-type metaquartz-syenite to -granite in the Eastern Anatolia: Implications for Late Ordovician-Silurian rifting at the northern margin of Gondwana



ELSEVIER

Contents lists available at ScienceDirect

Gondwana Research

journal homepage: www.elsevier.com/locate/gr



Silurian A-type metaquartz-syenite to -granite in the Eastern Anatolia: Implications for Late Ordovician-Silurian rifting at the northern margin of Gondwana



Gültekin Topuz ^{a,*}, Osman Candan ^b, Jia-Min Wang ^c, Qiu-Li Li ^c, Fu-Yuan Wu ^c, Ali Yılmaz ^d

- ^a İstanbul Teknik Üniversitesi, Avrasya Yer Bilimleri Enstitüsü, TR34469 Maslak, İstanbul, Turkey
- ^b Dokuz Eylül Üniversitesi, Jeoloji Mühendisliği Bölümü, Tınaztepe Yerleşkesi, Buca, İzmir, Turkey
- c State Key Laboratory of Lithospheric Evolution, Institute of Geology and Geophysics, Chinese Academy of Sciences, Beijing 100029, China
- ^d Cumhuriyet Üniversitesi, Çevre Mühendisliği Bölümü, 58140 Sivas, Turkey

ARTICLE INFO

Article history: Received 4 September 2020 Received in revised form 28 October 2020 Accepted 5 December 2020 Available online 09 December 2020

Keywords:
A-type granite
Zircon Hf and oxygen isotopy
U-Pb zircon dating
Ocean island basalt
Anatolide-Tauride block
Turkey

ABSTRACT

The Anatolide-Tauride block in the Tethyan belt represented passive northern continental margin of Gondwana throughout Paleozoic time. In this paper, we report on a relatively large amphibolite-facies metaquartz-syenite to -granite complex (~60 km²) in the Eastern Anatolia, the easternmost part of the Anatolide-Tauride block. Igneous textures in the metaintrusive complex are variably preserved. The preserved igneous minerals include mesoperthite + quartz \pm aegirine-augite \pm sodic amphibole \pm calcic amphibole \pm biotite and \pm allanite. Mesoperthite is the sole feldspar in well-preserved igneous textures, suggesting hypersolvus nature of the original quartz syenite to granite. In the well-recrystallized samples, mesoperthite is partially or totally replaced by discrete grains of plagioclase and K-feldspar. U-Pb dating on igneous zircons from three samples yielded Silurian igneous crystallization ages (430-440 Ma). All rock types have typical geochemical characteristics of A-type syenite to granite with relatively high abundances of FeO*, Na₂O, K₂O, Nb, Ga, Zr, Ce, and Zn, and low abundances of MgO, CaO and Sr, resulting in high ratios of Fe/Mg and Ga/Al. Geochemical features such as (i) the absence of negative Nb-Ta anomalies on multielement variation diagrams, (ii) the enrichment of Nb and Ce relative to Y, and (iii) Y/Nb, Yb/Ta and Ce/Nb ratios similar to those in ocean island basalts point to A₁-type syenite and granite which are thought to be differentiates of ocean island basaltic magmas. Estimated magma temperatures based on zirconium saturation range from 850 to 990 °C, indicating derivation of the original quartz syenite and granite from high-temperature juvenile magmas. Initial ϵ Hf values of the igneous zircons from two samples are 2.59 \pm 1.14 and 2.30 \pm 1.29, while δ^{18} O values of the zircons range from 5.41 to 7.32% with a median of 6.50 \pm 0.48%. All these isotopic characteristics suggest that the quartz syenite to granite were derived from high-temperature mantle magmas with insignificant crustal assimilation. The Late Ordovician-Silurian A-type igneous rocks in the northern part of the Anatolide-Tauride block were probably related to a rifting event at the northern margin of Gondwana, leading to the opening of the Paleo-Tethys. This interpretation is also supported from (i) regional geological features of the Early Paleozoic sedimentary successions suggestive of extensional setting during the Late Ordovician-Silurian, (ii) the presence of Silurian anorogenic magmatism in continental blocks detached from Gondwana during Early Paleozoic time, and (iii) the presence of Silurian deep sea sedimentary blocks in Paleo-Tethyan accretionary complexes.

 ${\hbox{$\mathbb{Q}$ 2020 International Association for Gondwana Research. Published by Elsevier B.V. All rights reserved.}\\$

1. Introduction

Within the Tethyan belt, the Anatolide-Tauride block was attached to Gondwana throughout the Paleozoic, forming its passive northern continental margin. Its detachment from Gondwana is thought to

E-mail addresses: topuzg@itu.edu.tr (G. Topuz), osman.candan@deu.edu.tr (O. Candan), wangjiamin@mail.iggcas.ac.cn (J.-M. Wang), liqiuli@mail.iggcas.ac.cn (Q.-L. Li), wufuyuan@mail.iggcas.ac.cn (F.-Y. Wu), ylmazali06@gmail.com (A. Yılmaz).

have occurred during the Early Triassic (Şengör and Yılmaz, 1981; Göncüoğlu et al., 2003; Uzunçimen et al., 2011; Akal et al., 2012) (Fig. 1). However, timings of the rifting of the Gondwanian blocks such as Avalonia (e.g. the Istanbul zone) and Armorica (e.g., the Sakarya zone) from Gondwana are not well-constrained (e.g., Okay et al., 2008a, 2008b; Okay and Topuz, 2017; Topuz et al., 2020; Ustaömer et al., 2012a, 2012b; Winchester and the Pace TMR Network Team, 2002). Here, we report on so far unknown Silurian A-type metasyenitic to -granitic rocks with an outcrop area of ca. 60 km² within the amphibolite-facies metamorphic rocks in the Eastern Anatolia, the

^{*} Corresponding author.

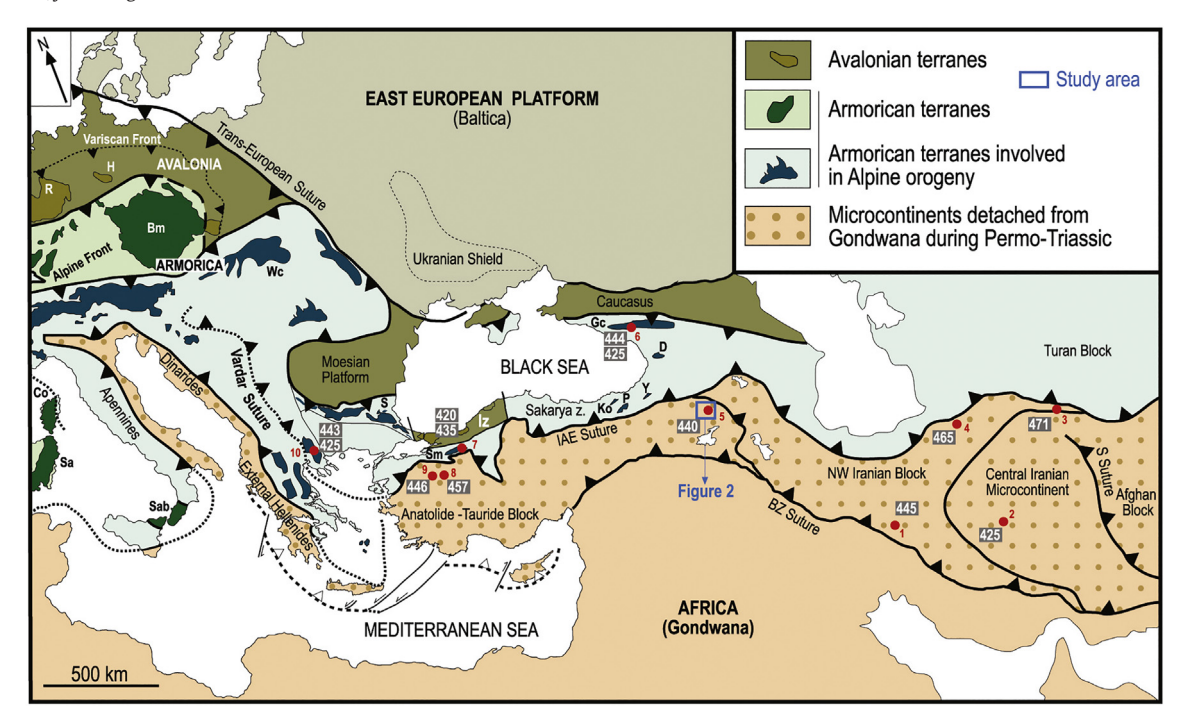


Fig. 1. Tectonic map of Europe and the Middle East, showing Phanerozoic sutures and continental blocks (modified from Schmid et al., 2008; Okay et al., 2008a-b; Topuz et al., 2020). Numbers stand for the radiometric ages of Ordovician to Silurian magmatism. ¹Shahsavari Alavijeh et al. (2018); ²Vesali et al. (2020), ³Moghadam et al. (2018), ⁴Moghadam et al. (2017); ⁵this study; ⁶Somin (2011); ⁷Topuz et al. (2020); ⁸Okay et al. (2008a); ⁹Özbey et al. (2013a, 2013b); ¹⁰Antić et al. (2016). The dark colored areas represent the main basement exposures. Bm: Bohemian massif; Co: Corsica; D: Dzirula; Gc: Greater Caucasus; H: Harz; Iz: Istanbul zone; Ko: Kurtoğlu; P: Pulur; R: Rhenisch massif; S: Strandja; Sab: Sicilian-Apulian basement; Sa: Sardinia; Sm: Saricakaya massif; Wc: Western Carpathians; Y: Yusufeli.

easternmost part of the Anatolide-Tauride block. Our data demonstrate that the metasyenite to -granite display A₁-type geochemical affinity, and were derived from the differentiation of juvenile, high-temperature ocean island basaltic magmas during Silurian time. Based mainly on regional stratigraphic constraints from the non-metamorphic part of the Anatolide-Tauride block and anorogenic nature of Late Ordovician to Silurian magmatism in both the Anatolide-Tauride block and the Sakarya zone, we suggest that the Silurian anorogenic granitic magmatism in the Anatolide-Tauride block formed in a rift setting probably related to the detachment of Armorica (e.g. the Sakarya zone) from Gondwana and the opening of the Paleo-Tethyan ocean.

2. Geological framework

The Anatolide-Tauride block is a Gondwana-derived continental block, and bounded by the Izmir-Ankara-Erzincan suture (IAES) to the north, and by the Bitlis-Zagros suture (BZS) to the south (Fig. 1). The Izmir-Ankara-Erzincan suture represents the trace of a long-lived oceanic domain from Silurian to end-Mesozoic time (Okay, 2000; Topuz et al., 2013, 2020). On the other hand, the Bitlis-Zagros suture represents the trace of the oceanic domain which first opened during Early Triassic time (Şengör and Yılmaz, 1981; Göncüoğlu et al., 2003; Uzunçimen et al., 2011; Akal et al., 2012). Thus, the Anatolide-Tauride block was a passive continental margin attached to the northern margin of the Gondwana throughout Paleozoic time. Its Paleozoic stratigraphy is characterized by carbonate and clastic sedimentary sequences (Özgül, 1976; Göncüoğlu and Kozlu, 2000; Monod et al., 2003) and rare igneous rocks of Ordovician, Carboniferous and Permo-Triassic ages (Okay et al., 2008a; Özbey et al., 2013a, 2013b; Akal et al., 2012; Candan et al., 2016). Large parts of the Anatolide-Tauride block were metamorphosed during Late Cretaceous, Paleocene and Eocene times (e.g. Sherlock et al., 1999; Candan et al., 2005; Pourteau et al., 2013; Schmidt et al., 2015). In clear distinction to the Anatolide-Tauride block, the Sakarya zone was already part of Laurussia during the Carboniferous, and is characterized by Carboniferous high-T/middle to low-P metamorphism, and Devonian, Carboniferous and Permian orogenic magmatism (e.g. Topuz et al., 2010, 2020; Okay and Topuz, 2017, and the references therein).

The East Anatolia, eastward extension of the Anatolide-Tauride block, is largely covered by Neogene to Quaternary volcanic and sedimentary rocks (e.g. Yılmaz and Yılmaz, 2019). This volcanic and sedimentary cover sits over a basement comprising (i) Late Cretaceous high-*T* / low- to middle-*P* metamorphic rocks, (ii) Late Cretaceous gabbroic, quartz monzonitic to tonalitic intrusions, and (iii) allochthonous Late Cretaceous ophiolitic mélanges and relatively intact ophiolites close to the Izmir-Ankara-Erzincan suture (Yılmaz et al., 1988, 2010; Topuz et al., 2017; Yılmaz and Yılmaz, 2019; Rolland et al., 2020). This basement crops out in several inliers beneath young volcanic and sedimentary cover. The Taşlıçay-Diyadin metamorphic rocks represent the second largest basement exposure (Fig. 2).

3. Taşlıçay-Diyadin metamorphic rocks

The Taşlıçay-Diyadin metamorphic rocks are exposed over an area of ~100 km², and are unconformably overlain by Neogene to Quaternary volcanic rocks (Fig. 2). To the northwest, the metamorphic rocks are intruded by an Early Miocene leucogranite (Açlan and Duruk, 2018; Açlan and Turgut, 2020; Topuz et al., 2019). The metamorphic rocks are represented by two tectonometamorphic units separated by a major fault: (i) an upper amphibolite-facies unit, and (ii) and greenschist-facies unit. The amphibolite-facies domain comprises a metaintrusive complex and a heterogeneous series consisting of metapelite, marble and quartzite with local intercalations of amphibolite. The metaintrusive complex, the subject of this study, ranges from metasyenite to –granite in composition, and makes up ca. 60% of the exposure area of the amphibolite-facies domain. The metapelites are characterized by local development of migmatitic domains and mineral assemblages

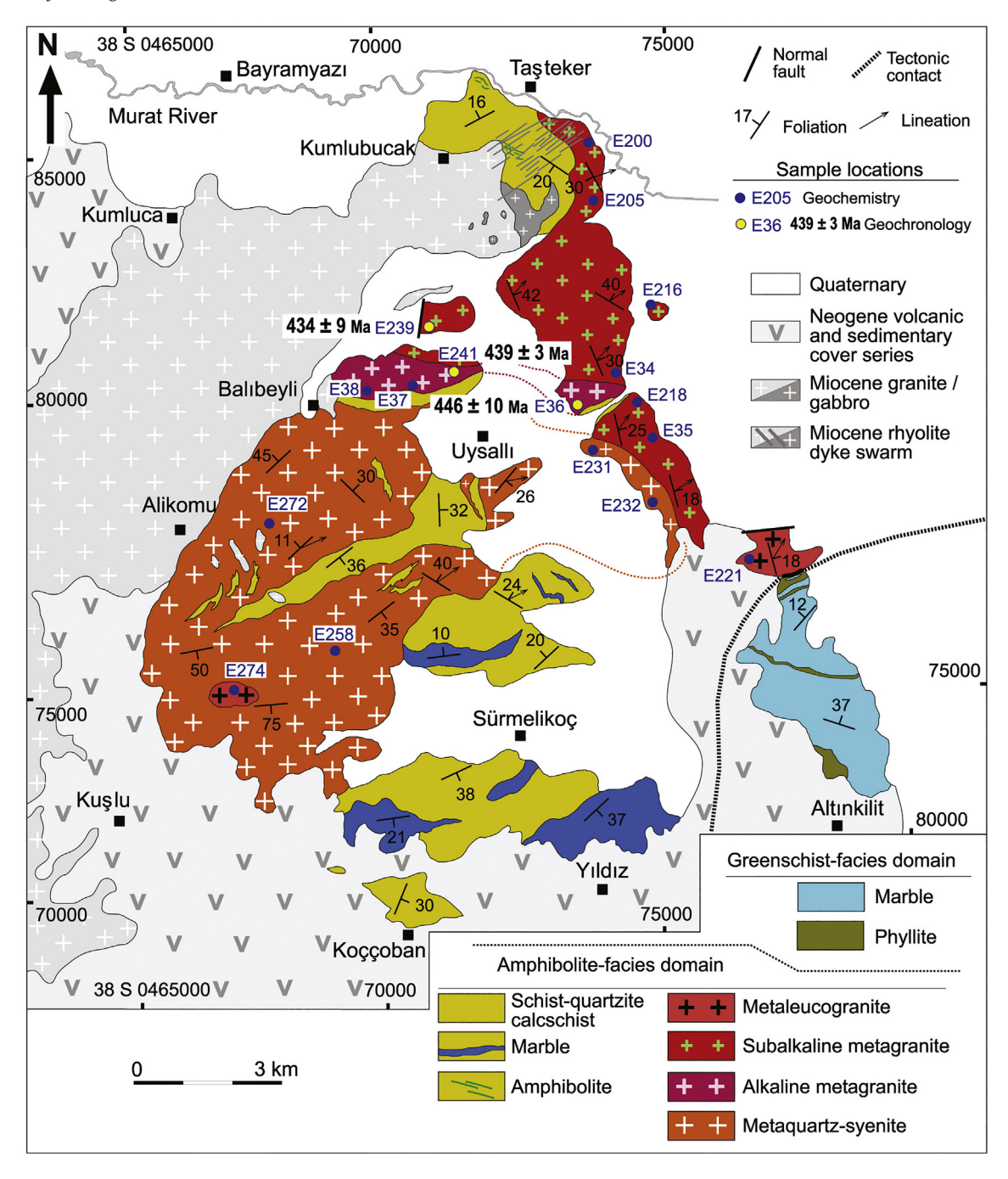


Fig. 2. Geological map of the Taşlıçay-Diyadin metaintrusive complex (Ağrı, Eastern Anatolia).

involving garnet, sillimanite, biotite, plagioclase and feldspar. The greenschist-facies domain consists mainly of platform-type marble (95% of exposure area) and minor phyllite (5%). The high-grade domain was derived from an Early Paleozoic rock assemblage, and the greenschist-facies domain, on the other hand, by an Early Mesozoic one, as deduced by U–Pb ages of the detrital zircons in one metaquartzite and one phyllite sample (Topuz et al., 2017, unpublished data). The rock assemblages of both the amphibolite-facies and the greenschist-facies domains can be correlated with the Early Paleozoic and Early Mesozoic rock assemblages in the non-metamorphic parts of the Anatolide-Tauride block (Özgül, 1976; Göncüoğlu and Kozlu, 2000; Monod et al., 2003; Ghienne et al., 2010). On the basis of the protolith ages of the metamorphic rocks and analogy to the neighboring

Akdağ metamorphic complex, ca. 75 km to west (Topuz et al., 2017), a Late Cretaceous metamorphic age is regarded plausible.

The metaquartz-syenite to -granite complex forms a NE-SW trending body, ~9 km long and ~ 5 km across within the metasedimentary rocks consisting of metapelite, quartzite, marble and calc-silicate gneiss (Fig. 2). Within the country metasedimentary rocks, there are up to several meter-thick veins of the metasyenite to -granite. All the rock types of metasyenite to -granite complex are felsic, equigranular with a greyish to pinkish white color. Mafic minerals, e.g. amphibole, clinopyroxene, biotite and Fe–Ti oxide, are invariably less than 20 vol%. The rocks are either massive (Fig. 3a) or foliated with variably developed stretching lineation (Figs. 3b-d). At the northeastern boundary, the rock types display a pronounced mylonitic foliation

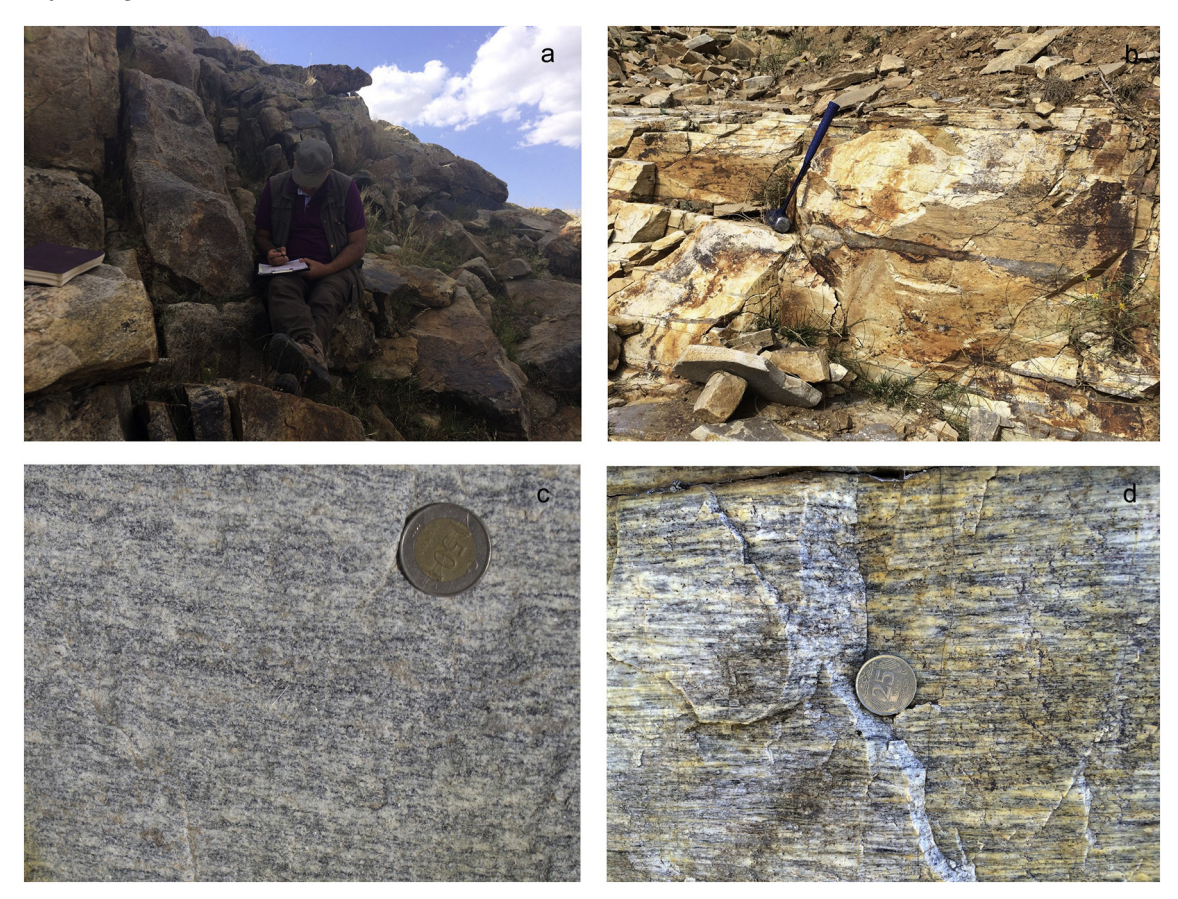


Fig. 3. Field pictures of the Taşlıçay-Diyadin metaintrusive complex (Ağrı, Eastern Anatolia). a Some massive boulders of the metaquartz-syenite. The outcrop shows a rusty pinkish weathering color. b Foliated metagranite with foliation-parallel quartz vein. c Greyish white fresh surface of the slightly foliated metagranite. The coin is 2.39 cm across. d Strongly mylonitized domain of the metagranite. The coin is 2 cm across.

striking NNW-SSE with stretching lineation plunging to NE (Fig. 2). In the central to southwestern part, the foliation strikes NE-SW. We could not recognize any mafic domain in the metasyenite to –granite complex, which could be interpreted as the premetamorphic mafic microgranular enclaves. There are up to 80 cm thick foliation-parallel veins of quartzite (Fig. 3b). Despite the amphibolite-facies metamorphism, igneous textures and minerals are well-preserved. The different rock types are not distinguishable from each other in the field. Boundaries of distinct rock types in Fig. 2 are drawn in an approximate way, based on the petrography of investigated samples in concert with bulk rock compositions. The dominant rock type is metaquartz-syenite, cropping out mainly in the central and southwestern part of the intrusion. The metagranite is exposed to the northeast and northern part.

The rock types in the metaintrusive complex range from metaquartz-syenite to highly evolved metaleucogranite (Table A1). Primary igneous textures are variably preserved. In the massive and feebly foliated samples, primary igneous textures and minerals are wellpreserved. Preserved igneous texture is defined by fine-grained, unoriented, equigranular intergrowth of mesoperthite and quartz (Fig. 4a-b). The igneous minerals are mesoperthite, quartz, \pm aegirine-augite, \pm sodic amphibole, \pm calcic amphibole, \pm biotite, \pm allanite, \pm flourite, and titanomagnetite. Feldspars in samples with well-preserved igneous textures are represented merely by mesoperthite (Fig. 4a-b), pointing to hypersolvus nature of the original quartz syenite to granite complex, namely crystallization at relatively low vapor pressures (Gill, 2011, p. 264). Zircon, apatite and titanite are common accessory minerals. Aegirine-augite and sodic amphibole are confined to samples E218 and E258, and calcic amphibole in samples E37 and E272 (Tables A1 and A2). Titanomagnetite commonly forms elongated grains along the foliation plane, and are surrounded by a reaction rim of titanite. Mineralogical differences among the rock types (metaquartz-syenite to -leucogranite) are defined by modal abundance of feldspar with respect to quartz. The metaquartz-syenite is characterized by elevated modal amount of mesopertite (ca. 70-80 vol%), whereby modal amount of guartz is between 5 and 14 vol%. Metaleucogranite, on the other hand, contains the highest amount of guartz (37–30 vol%), and lesser amount of feldspar relative to the other rock types. In the well-foliated samples, mesoperthite is replaced by discrete grains of K-feldspar and plagioclase (Figs. 4c-f). Some well-foliated samples may contain relics of mesoperthite. Biotite is the main metamorphic ferromagnesian mineral in the well-foliated mylonitic samples. Foliation is defined by parallel alignment of biotite and elongated ribbons and high concentration of titanomagnetite along the foliation plane. Locally zircon, titanite and -titanomagnetite are concentrated along the foliation planes. All the microtextural features of mylonitic samples and mineral assemblages are characteristic of amphibolite-facies conditions.

4. Analytical techniques

For bulk-rock analyses about 5 kg of metaquartz-syenite to -granite were first processed in a steel jaw crusher. An aliquot of about 30 g was powdered in an agate rind-disc mill. Rock powders were then dried at 105 °C for ca. 24 h. Whole rock analysis were performed at ACME Analytical Laboratories Ltd. in Vancouver (Canada) using a ICP emission spectrograph (Jarrel Ash 219 AtomComb 975) for major elements and trace elements Ba, Nb, Ni, Sr, Sc, Y and Zr, and ICP mass spectrometer (Perkin-Elmer Elan 6000) for the other trace elements inclusing rare

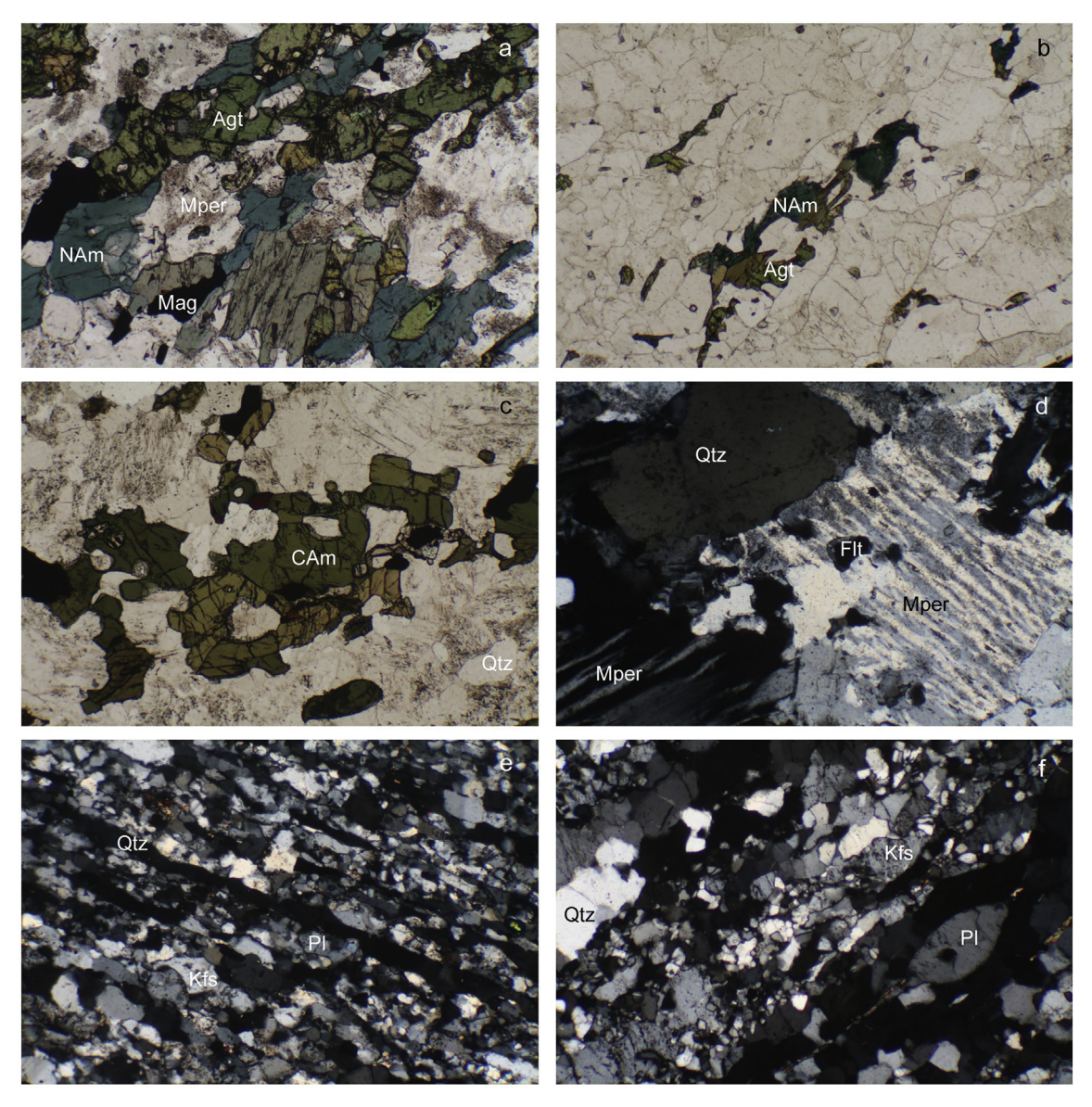


Fig. 4. Thin section micrographs showing the mineral constituents and microtextural features of the different rock types from the Taşlıçay-Diyadin metaintrusive complex. a Preserved igneous aegirine-augite (Agt) and sodic amphibole (NAm) coexist with titanomagnetite (Mag), mesoperthite (Mper) in metaquartz-syenite (sample E258), b Igneous aegirine-augite (Agt) and sodic amphibole (NAm) in subalkaline metagranite (sample E218), c Igneous calcic amphibole (CAm) coexisting with titanomagnetite, mesoperthite and quartz in metaquartz-syenite (sample E272), d Mesoperthite with inclusions of fluorite in subalkaline metagranite (sample E243), e Quartz ribbons and discrete grains of plagioclase and K-feldspar in mylonitized alkaline metagranite (sample E34). Note that all mesoperthite is replaced by plagioclase and K-feldspar. f Quartz, plagioclase and K-feldspar together with tiny flakes of biotite and muscovite in mylonitized subalkaline metagranite (sample E34). The long edge of micrographs is equal to 1.5 mm in thin section.

earth elements. Analytical procedure and uncertainties are the same as described in Topuz et al. (2019).

Mineral separation was performed at the Avrasya Yer Bilimleri Enstitüsü in Istanbul by conventional techniques involving breaking, sieving, washing, magnetic and heavy liquid separation. After the heavy liquid separation, the zircons were handpicked and placed on a double-sided band under binocular. After embedding into epoxy, the mount was polished to reveal the internal structures of the zircon and potential inclusions. The internal structures were revealed by cathode-luminescence imaging at the Jeoloji Mühendisliği Bölümü (Hacettepe) in Ankara. U–Pb analyses and trace element compositions of zircon were obtained using a laser ablation inductively coupled plasma mass spectrometer (LA-ICP-MS) at the Institute of Geology and Geophysics, Chinese Academy of Sciences (IGGCAS), which couples a pulsed 193-nm ArF Excimer laser system with an Agilent 7700 ICP-MS. During the analyses, a 50–100 mJ energy at a repetition rate of 6 Hz was used. A

large spot size of 35 μ m was used during the measurements. Each analysis measures the background for ~30 s before switching on the laser for ~40 s. Reference material was analyzed each tenth analysis. Data reduction, including corrections for baseline, instrumental drift, mass bias and downhole fractionation were calculated using Glitter software 4.15. Zircon standard 91,500 was used as internal standard. Analysis of GJ-1 standard as the external standard gave an age value of 597 \pm 4 Ma ($n=9,2\sigma$, MSWD = 0.98). Trace elements of zircon were obtained simultaneously during the U-Pb analyses. Trace element calibration was performed relative to NIST 610 glass. Accuracy and precision of the analyses were evaluated with respect to a BCR secondary glass standard and are always better than 10% combined. U-Pb age calculations were performed by Isoplot 4.15 software (Ludwig, 2003). The analytical data are listed in Table A2.

Hafnium and oxygen isotopic determinations on zircons were on NEPTUNE multicollector ICP-MS equipped with a Geolaser 193 laser ablation system and CAMECA IMS 1280 SIMS at the Institute of Geology and Geophysics, Chinese Academy of Sciences (IGGCAS, Beijing), respectively. The analytical conditions are the same as described in Topuz et al. (2019). Hafnium isotopic compositions of zircon grains have been measured on the dated zircons from two metagranite samples (samples E36, E241). The analytical data are listed in Table A3. Twenty grains of zircon were analyzed from each sample. During the measurement sessions, twenty analyses of Mud Tank zircon and ten analyses of Plesovice zircon yielded average $^{176}\mathrm{Hf}/^{177}\mathrm{Hf}$ values of 0.282467 \pm 0.000026 and 0.282447 \pm 0.000021, respectively. Oxygen isotopic compositions of the zircon have been measured on the igneous

zircons from one samples (E36). Twenty zircon grains were measured for $\delta^{18}\text{O}$ compositions (Table A4). During the measurement session, 40 grains of the Penglai zircon were also measured, yielding $\delta^{18}\text{O}$ values 5.27 \pm 0.21%.

5. Bulk rock geochemistry

Sixteen samples from the metaintrusive complex have been analyzed for major and trace element compositions (Table 1). As the rocks underwent amphibolite-facies metamorphism, effect of the amphibolite-facies metamorphism on the bulk rock composition should

Table 1Major and trace element compositions of metaquartz-syenite to metaleucogranite from the Taslıcay-Diyadin metaintrusive complex (Ağrı, Eastern Anatolia).

Sample	E232	E258	E231	E272	E36	E37	E38	E34	E35	E200	E205	E216	E218	E243	E221	E274
Rock type	QS	QS	QS	QS	AG	AG	AG	SA	SA	SA	SA	SA	SA	SA	LG	LG
SiO ₂	63.76	62.44	68.32	69.11	70.85	71.33	71.93	76.65	77.74	77.77	75.45	77.19	75.15	76.42	77.50	78.34
TiO ₂	0.78	1.24	0.79	0.35	0.34	0.34	0.39	0.18	0.18	0.17	0.20	0.09	0.23	0.15	0.19	0.12
Al_2O_3	16.55	14.45	15.68	14.55	14.76	13.53	14.49	11.81	10.84	11.17	12.04	11.84	11.89	12.38	11.72	11.47
Fe ₂ O ₃ total	5.63	6.41	2.75	4.15	2.72	3.09	1.69	1.72	2.29	1.90	2.58	1.30	2.59	1.45	1.42	1.11
MnO	0.08	0.21	0.03	0.10	0.03	0.11	0.04	0.01	< 0.01	0.03	0.05	0.02	0.08	0.01	0.03	0.02
MgO	0.60	0.91	0.52	0.28	0.07	0.12	0.02	0.10	< 0.01	0.11	0.18	0.08	0.01	< 0.01	0.05	0.05
CaO	0.50	1.10	0.21	0.83	0.78	0.66	0.26	0.13	0.03	0.12	0.47	0.45	0.19	0.28	0.05	0.11
Na ₂ O	5.95	6.82	6.00	4.65 5.40	4.70	4.66	4.79	3.83	3.48	3.51	3.67	3.75	4.52	4.07	3.58	3.35
K ₂ O P ₂ O ₅	5.39 0.10	5.19 0.37	4.95 0.15	0.03	5.01 0.03	5.11 0.05	5.48 0.04	4.63 0.02	4.62 <0.01	4.51 0.02	4.85 0.01	4.60 0.02	4.67 0.01	4.92 <0.01	4.90 <0.01	4.87 <0.01
LOI	0.10	0.40	0.13	0.03	0.40	0.70	0.60	0.80	0.60	0.50	0.30	0.50	0.40	0.10	0.30	0.40
Total	99.71	99.74	99.80	99.76	99.69	99.74	99.70	99.90	99.82	99.85	99.82	99.86	99.78	99.84	99.79	99.89
Sc	1.00	6.00	6.00	8.00	7.00	8.00	10.00	3.00	1.00	<1	2.00	<1	2.00	1.00	2.00	1.00
Ni	82.2	72.8	29.2	38.0	1.00	0.700	0.400	0.700	1.10	38.6	57.2	73.9	54.3	67.3	77.5	63.1
Co	2.10	2.50	0.500	0.700	1.90	0.600	0.400	0.700	0.400	1.10	1.00	1.00	0.600	1.80	1.60	0.900
V	<8	34	24	<8	15.0	8.00	<8	<8	<8	<8	<8	<8	<8	<8	9.00	<8
Ga	42.7	37.1	31.3	28.3	26.2	25.1	25.1	23.4	28.2	26.1	29.2	31.9	30.6	31.4	32.1	24.6
Zn	81.0	30.0	46.0	97.0	26.0	43.0	62.0	57.0	84.0	68.0	114	103	25.0	159	16.0	15.0
Cs	1.10	0.500	0.400	1.60	0.800	0.400	0.200	0.700	0.500	0.900	0.400	2.00	1.30	0.400	0.500	0.300
Rb	123	122	94.0	102	87.4	70.6	61.6	99.9	138	99.3	107	186	130	178	221	156
Ba	89	1341	746	837	923	929	850	82	10	75	27	49	26	110	19	13
U	4.40	2.30	2.50	2.40	2.80	0.800	1.40	1.60	6.10	1.60	2.70	6.10	3.10	6.30	9.40	6.20
Th Pb	23.9 0.800	10.5 7.20	12.2 1.10	17.7 1.50	18.8 0.700	9.80 1.50	9.60 1.80	12.4 2.70	26.4 8.70	16.3 1.70	15.4 0.500	24.8 1.00	23.2 3.90	19.3 5.50	19.8 3.00	18.9 1.20
Sr	35.1	104.1	84.1	72.3	86.9	68.7	76.3	21.2	13.1	28.1	21.3	13.0	6.30	18.0	30.7	17.7
Nb	238	175	112	80.7	78.5	55.6	58.5	65.2	145	79.1	84.1	118	97.6	107	251	128
Ta	12.8	8.6	6.5	3.4	4	2.7	2.4	4.3	11.2	5	5.1	10.1	6.8	4.7	19.5	7.6
Zr	1179	696	593	840	775	714	806	413	825	579	695	402	821	519	1096	526
Hf	27.1	16.4	13.3	19.3	18.5	14.4	16.0	10.4	23.8	13.8	16.5	16.5	22.1	17.2	33.9	17.7
Y	39.3	84.3	42.4	49.5	42.4	33.3	18.1	27.0	77.6	24.8	52.0	80.0	57.9	74.1	45.6	55.4
La	121	96.0	136	144	166	75.9	134	43.6	53.4	78.1	92.1	50.3	129	56.5	6.00	3.80
Ce	234	204	268	288	319	169	269	92.4	104	167	201	108	240	111	10.0	7.30
Pr	25.3	24.1	32.2	32.8	38.4	18.8	29.8	10.6	14.9	18.7	21.8	13.7	30.8	14.0	1.77	1.89
Nd	83.9	94.7	117	123	149	72.7	111	39.7	58.4	68.6	80.7	52.5	118	52.8	7.8	10.5
Sm	13.7	17.6	19.0	20.4	24.5	12.0	15.3	7.06	14.0	11.0	14.9	12.4	20.6	12.3	3.54	5.13
Eu	2.24	5.12	4.01	2.97	3.82	2.35	2.55	0.650	0.680	0.830	0.760	0.570	1.16	0.770	0.400	0.220
Gd	10.3	17.0	13.4	15.6	17.9	8.85	8.61	5.73	15.1	7.29	12.4	11.9	16.9	12.4	4.73	7.65
Tb Dy	1.55 8.57	2.69 15.9	1.83 9.46	2.13 11.1	2.45 11.6	1.33 7.35	0.970 4.66	0.940 5.62	2.77 16.6	1.00 5.62	1.90 11.5	2.17 13.6	2.37 13.1	2.22 13.9	1.03 7.62	1.67 11.0
Но	1.56	3.02	1.66	2.04	1.78	1.28	0.65	1.06	3.21	1.09	2.17	2.98	2.47	2.86	1.73	2.46
Er	4.65	8.23	4.24	5.29	4.69	3.50	1.78	3.09	8.79	3.06	6.49	8.61	6.99	8.48	6.02	7.03
Tm	0.650	1.03	0.580	0.740	0.660	0.470	0.250	0.460	1.29	0.480	0.910	1.26	0.950	1.20	1.11	1.01
Yb	4.39	5.99	3.64	4.97	4.62	3.23	1.76	3.24	8.23	2.90	5.76	8.06	6.17	7.20	8.39	6.58
Lu	0.630	0.800	0.540	0.810	0.660	0.510	0.270	0.480	1.22	0.480	0.860	1.14	0.920	1.01	1.29	0.960
Fe#	0.89	0.86	0.83	0.93	0.97	0.96	0.99	0.94	-	0.94	0.93	0.94	1.00	_	0.96	0.95
K20/Na20	0.91	0.76	0.83	1.16	1.07	1.10	1.14	1.21	1.33	1.28	1.32	1.23	1.03	1.21	1.37	1.45
ASI	1.00	0.77	1.00	0.97	1.01	0.94	1.01	1.02	1.01	1.03	0.99	0.99	0.93	0.99	1.04	1.04
mol KN/A	0.94	1.17	0.97	0.93	0.89	0.98	0.95	0.96	0.99	0.95	0.94	0.94	1.05	0.97	0.96	0.94
Nb/Ta	18.6	20.3	17.2	23.7	19.6	20.6	24.4	15.2	12.9	15.8	16.5	11.6	14.4	22.7	12.9	16.9
Zr/Hf	43.49	42.44	44.60	43.52	41.89	49.60	50.34	39.72	34.66	41.98	42.15	24.33	37.13	30.18	32.33	29.71
Tot REE	512.52	496.28	612.21	654.31	744.57	376.90	580.64	214.61	302.64	365.62	453.63	287.54	590.05	297.05	61.43	67.18
(La/Yb) _{cn}	18.58	10.81	25.26	19.52	24.24	15.84	51.37	9.07	4.37	18.16	10.78	4.21	14.14	5.29	0.48	0.39
(Gd/Yb)cn	1.88	2.29	2.98	2.53	3.13	2.21	3.95	1.43	1.48	2.03	1.73	1.19	2.20	1.38	0.45	0.94
Eu/Eu*	0.58	0.90	0.77	0.51	0.56	0.70	0.68	0.31	0.14	0.28	0.17	0.14	0.19	0.19	0.30	0.11

QS Metaquartz-syenite; AG Alkaline metagranite; SA Subalkaline metagranite; LG Metaleucogranite; Fe# = molecular Fe0*/(molecular Fe0* + molecular Mg0); cn: chomdrite normalized; $Eu/Eu^* = Eu_{cn}/(Sm_{cn}^*Gd_{cn})^{0.5}$; ASI (Aluminium Saturation Index) = molecular $Al_2O_3/(Na_2O+K_2O+CaO)$; mol $KN/A = molecular K_2O+Na_2O/Al_2O_3$.

be taken into account. Generally, elements such as Na, K, Ca, Rb, Sr and Ba (large ion lithophile elements, LILE) are thought to be highly mobile during metamorphic processes (e.g., Polat and Hofmann, 2003). Rare earth elements (REE), high-field strength elements (HFSE, Th, Nb, Ta, Zr, Hf and Ti) and transitional metal elements (Sc, V, Cr and Ni) are regarded as relatively immobile during metamorphism, away from the fluid focused domains such as quartz veins (e.g. Polat and Hofmann, 2003; Ague, 2017). Exceptional care has been given during the sampling for the geochemical analysis. Samples were taken mainly from the massive to less deformed domains, away from any veins or lithological contacts.

The loss on ignition values are consistently low (0.10–0.80 wt%) (Table 1). On the variation diagrams (Figs. 5a and 6), even the fluid mobile elements such as Ca, Na and K show well-defined fractionation trends against silica. In addition, mostly subparallel trends and uniform contents of the LILE, HFSE and REE suggest that the element mobility during the amphibolite-facies metamorphism was insignificant in most samples. Samples display a wide-ranging compositional variation $(SiO_2 = 62-78 \text{ wt\%}; Al_2O_3 = 11-17 \text{ wt\%}; Na_2O = 3-7 \text{ wt\%})$. On the SiO_2 vs Na₂O + K₂O diagram after Middlemost (1994), samples define a linearly decreasing trend from strongly alkaline to subalkaline compositions, falling into the fields of syenite through quartz monzonite and alkaline granite to subalkaline granite (Fig. 5a). This trend is similar to the differentiation trend defined by the mildly alkaline anorogenic rocks in the Kenya rift valley (see Gill, 2011, p. 321). Hereafter, the rocks names which are based on the combination of petrography and chemical composition (e.g., metaquartz-syenite, alkaline metagranite, subalkaline metagranite and metaleucogranite) are used. As the samples plotting into syenite and quartz monzonite (Fig. 5a) do contain igneous quartz, and do not differ from each other in terms of modal mineralogy, they are collectively called as metaquartz-syenite. The alkaline metagranite -differs from subalkaline metagranite in higher feldspar contents. The metaleucogranite is characterized by the highest quartz content and lowest contents of ferromagnesian minerals. The K₂O/Na₂O ratio varies from 0.76 to 1.45, systematically increasing from metaquartz-syenite through alkaline metagranite and subalkaline metagranite to metaleucogranite (Table 1). The aluminum saturation indices (molecular $Al_2O_3/(CaO + K_2O + Na_2O)$) range from 0.77 to 1.04, suggesting metaluminous to weakly peraluminous affinity (Fig. 5b). Two aegirine-augite and sodic amphibole-bearing samples (E218 and E258) are peralkaline. The variation of the aluminum saturation indices among the rock types is not systematic. Samples of the metaquartz-syenite to metagranite are peralkaline through metaluminous to peralkaline (Fig. 5b).

Overall, the samples are characterized by relatively high abundances of Fe₂O₃*, Na₂O, K₂O, Zr, Nb, Ga, Y and Ce, and relatively low abundances of MgO, CaO and Sr as well as resulting high ratios of FeOtot/ (FeO_{tot} + MgO) and Ga/Al (Fig. 1; Figs. 6a-b). These geochemical features are diagnostic for A-type (ferroan) granites (e.g., Loiselle and Wones, 1979; Whalen et al., 1987; Eby, 1990, 1992; Frost and Frost, 1997, 2011; Frost et al., 1999, 2001; Bonin, 2007). On the basis of Nb, Y and Ce concentrations, samples are characterized by relatively Y-poor, and Nb- and Ce-rich compositions, falling into the field of A₁-type granites of Eby (1992), which are thought to have derived from the differentiation of the ocean island basalt-like magmas (Fig. 6c). Major element geochemical data display a coherent array on variation diagrams. Abundances of TiO₂, Al₂O₃, Fe₂O₃*, CaO, Na₂O, Ba and Sr roughly decreases with increasing abundances of SiO₂ (Fig. 7). Abundances of Fe₂O₃*, MgO, P₂O₅, Rb, Ga, Nb and Ta decrease from metaguartz-syenite to alkaline metagranite with increasing silica, but do not show any linear relationship in subalkaline metagranite and metaleucogranite. This state suggests that the abundances of these elements are controlled by mineral fractionation in metaguartz-syenite and alkaline metagranite, and the subalkaline metagranite and metaleucogranite are not related to quartz syenite and alkaline granite by mineral fractionation. The metaquartz-syenite to alkaline metagranite display shoshonitic affinity, and subalkaline metagranite and metaleucogranite high-K calc-alkaline affinity (Fig. 7).

On the chondrite-normalized (cn) REE patterns, samples of both the metaquartz-syenite and alkaline metagranite display similar comparable patterns characterized by strongly fractionated light REEs with respect to heavy ones (La/Yb_{cn} ~ 16–51) with variably negative Eu anomalies (Eu/Eu* = Eu_{cn}/(Sm_{cn}Gd_{cn})^{0.5} = 0.52–0.90) (Figs. 8a-b; Table 1). A slight concave-upward (spoon-shaped) form is recognizable in the patterns. The subalkaline metagranites, on the other hand, have slightly fractionated REE patterns (La/Yb_{cn} ~ 4–18) with pronounced negative Eu anomalies (Eu/Eu* ~ 0.14–0.31) (Fig. 8c). The metaleucogranites have the lowest REE concentrations. In clear distinction to the other rock types, the light rare earth elements are depleted with respect to heavy REEs (La/Yb_{cn} ~ 0.4–0.5; Fig. 8d), requiring the

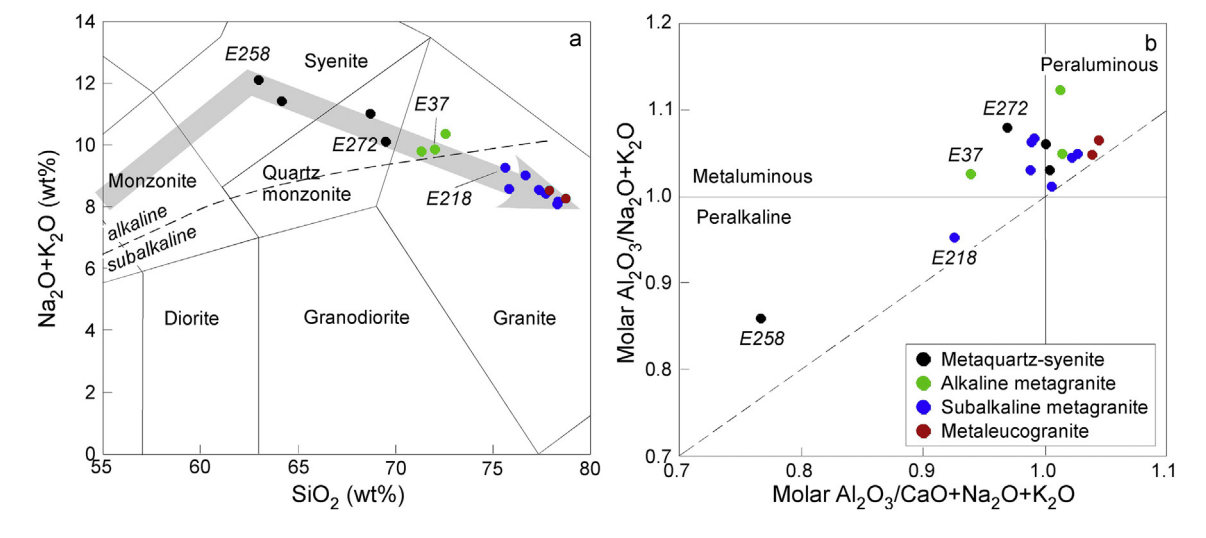
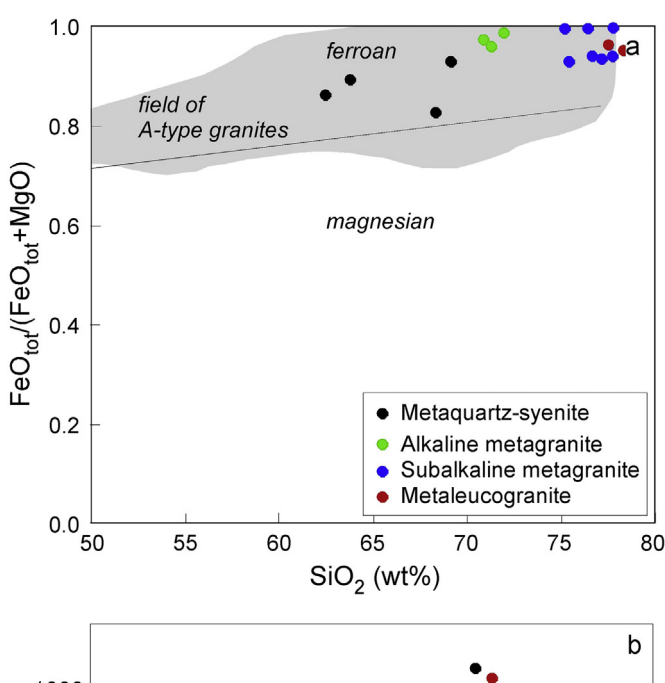
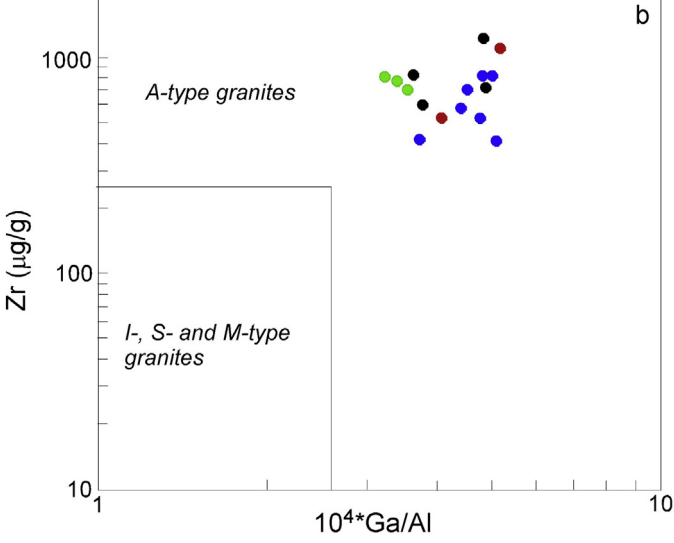
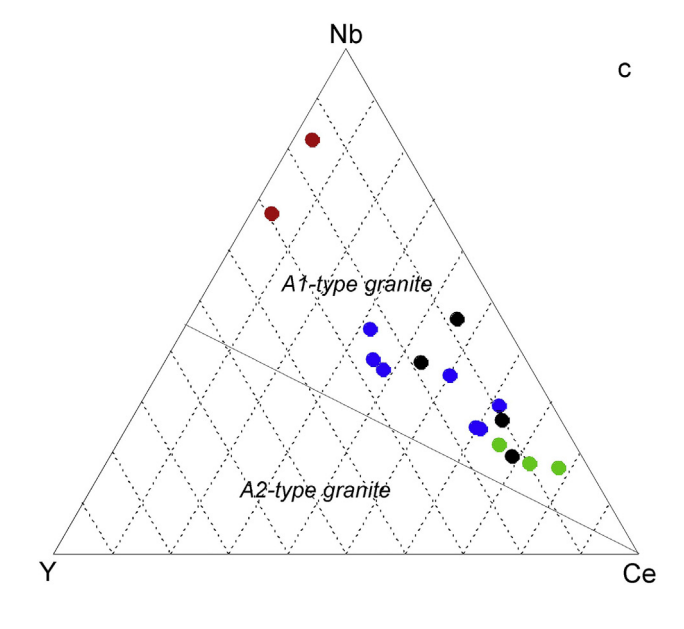


Fig. 5. a Compositional variation of the metaquartz-syenitic to metagranitic rocks from the Taşlıçay-Diyadin metaintrusive complex in the SiO₂ vs Na₂O + K₂O classification diagram after Middelmost (1994). The analyses were recalculated on water-free basis. The dashed line separates the alkaline and subalkaline series (taken from Irvine and Baragar, 1971). The shaded arrow shows the differentiation trend of mildly alkaline rocks from the Kenya rift (Gill, 2011, p. 321). Samples E258 and E218 are sodic amphibole-bearing, while samples E37 and E272 are calcic amphibole-bearing. b Distribution of the metaquartz-syenitic to metagranitic rocks from the Taşlıçay-Diyadin metaintrusive complex in molecular $Al_2O_3/CaO + Na_2O + K_2O$ vs molecular $Al_2O_3/Na_2O + K_2O$ diagram after Shand (1943), distinguishing peralkaline, metaluminous and peraluminous compositions.







differentiation of a light REE-enriched mineral such as allanite and titanite. On the multi-element variation diagrams normalized to primitive mantle after Sun and McDonough (1989), all the rock types are devoid of any negative Nb–Ta anomalies, in line with their anorogenic nature (Figs. 9a-d). Both metaquartz-syenite and alkaline metagranite are characterized by marked negative anomalies of Pb, Sr, P and Ti (Figs. 9a-b). Sample 232 differs from the other samples by the presence of pronounced negative Ba anomaly. In marked difference to metaquartz-syenite and alkaline metagranite, the subalkaline metagranites show additionally pronounced negative anomalies of Ba and Eu (Fig. 9c). Due to the hardly fractionated nature of rare earth elements, the multi-element variation diagram of the metaleucogranites differ in pattern from the other rocks and by the presence of positive Zr anomaly (Fig. 9d).

6. U-Pb zircon dating

To constrain the time of the igneous crystallization of the metaquartz-syenite to metagranite, laser ablation inductively coupled plasma mass spectrometry (LA-ICP-MS) U-Pb dating have been performed on zircon grains from three samples (alkaline metagranite: E36B and E241; subalkaline metagranite: E239) (see Fig. 2 for sample locations). Sample E36B and E241 are alkaline metagranites, comprising quartz, feldspar and minor biotite as well as accessory zircon and apatite. Samples E239 is a poorly foliated subalkaline metagranite in which igneous textures and minerals are relatively well-preserved. Apart from quartz and mesoperthite, they include biotite, allanite and \pm calcic amphibole and accessory phases such as apatite and zircon. From each sample, thirty grains of zircon are analyzed for both U-Pb-Th isotopic and trace-element compositions (Table A2).

Overall, the zircons from all the three samples are fairly equivalent grains characterized by oscillatory zoned rims overgrowing on either dark- or bright-luminescent unzoned cores (Fig. 10). A wide array of mineral inclusions is found in zircons, including quartz, albite, apatite, allanite (Ce,Ca,Y,La)₂(Al,Fe⁺³)₃(SiO₄)₃(OH), thorite ((Th,U)SiO₄), thorianite (ThO₂), fergusonite-(Y) (REENbO₄), bastnäsite ((Ce, La)CO₃F) and fluorbritholite (Ca,Ce,La,Na)₅(SiO₄,PO₄)₃(OH,F). After the screening the zircon analysis with inclusions, the Th and U concentrations of the dated grains are 37–229 and 75–367 µg/g, respectively (Table A2). The resulting Th/U ratios range from 0.33 to 0.93. The zircons are characterized by strongly fractionated chondrite-normalized rare earth element pattern with Lu/Gd_{cn} ratios of 8–17 and pronounced negative Eu anomaly (Eu/Eu* ~ 0.06-0.28) and pronounced positive Ce anomaly (Ce/ Ce* ~ 6–165) (Table A2). Inclusions usually leads to disappearance of Ce anomaly and increase of light rare earth element concentrations. The negative Eu anomalies suggest growth in the presence of feldspar. Both geochemical and morphological features of the dated zircons are suggestive of growth from a melt phase in the presence of feldspar. Obviously metamorphic overgrowths on the zircon grains are absent.

On the concordia diagrams of the analyzed zircon grains from the three samples, basically two linear are recognizable (Fig. 11). One trend is defined by nearly constant ²⁰⁶Pb/²³⁸U ratios and variable ²⁰⁷Pb/²³⁵U ratios. These data points have variable P, Ca, and higher light rare earth element concentrations, suggesting that this is caused by presence of inclusions with common Pb (Table A2). The second trend is defined by concordant to discordant data points with lower age values, ascribed to Pb loss during the metamorphism or a later event. During the age calculations, we have excluded the grains defining both trend, and regarded only concordant data points with concordance values, defined by ²⁰⁶Pb/²³⁸U age divided by ²⁰⁷Pb/²³⁵U age, between

Fig. 6. Distribution of the samples from the Taşlıçay-Diyadin metaintrusive complex in the discrimination diagrams. a SiO_2 vs $FeO_{tot}/FeO_{tot} + MgO$ after Frost et al. (2001), b $10^{4*}Ga/A$ l vs Zr after Whalen et al. (1987), and c Nb-Y-Ce triangular diagram after Eby (1992).

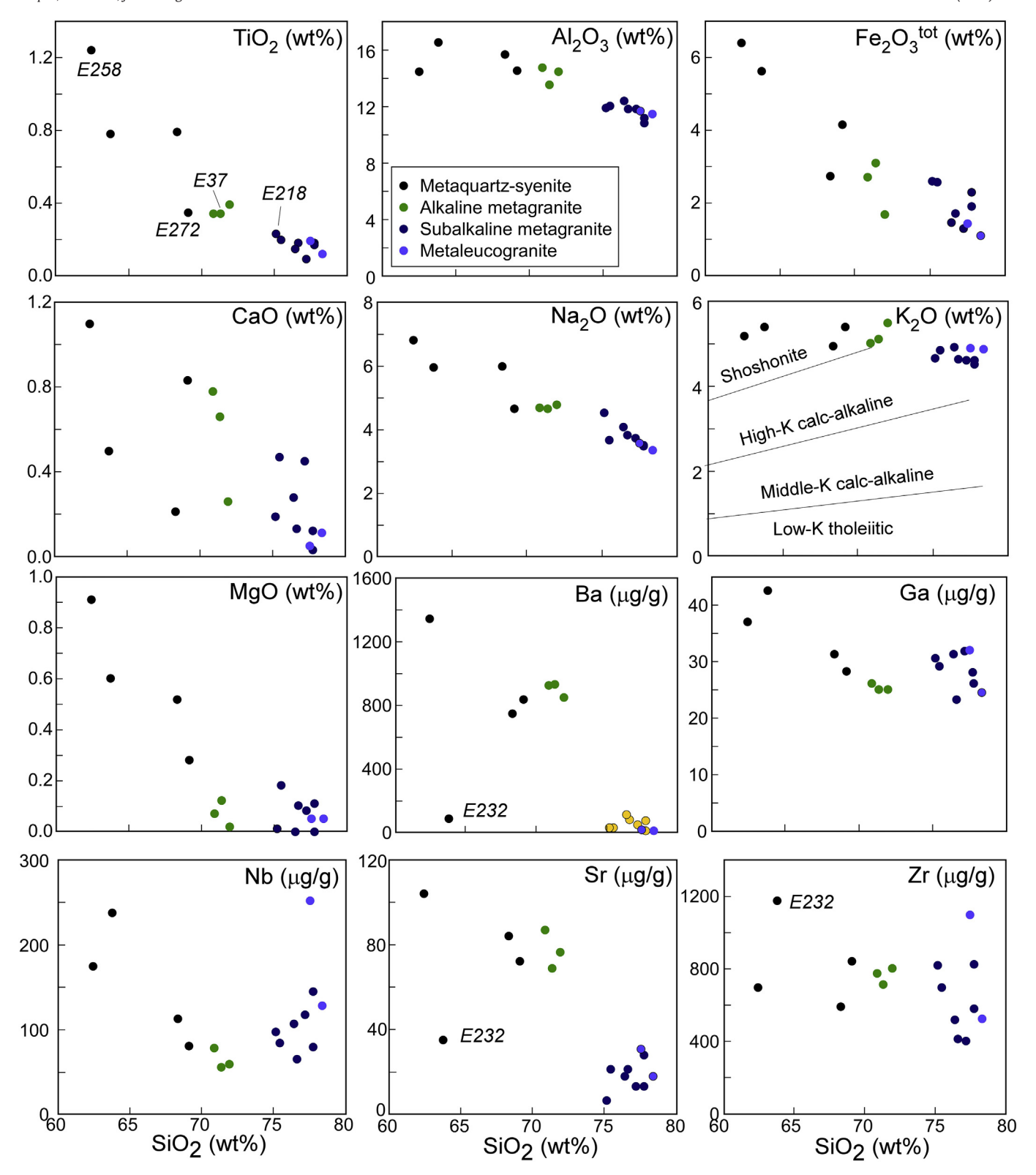


Fig. 7. Selected Harker variation diagrams for the samples from the Taşlıçay-Diyadin metaintrusive complex. Lines separating low-K, middle-K and high-K calc-alkaline and shoshonitic series are after Peccerillo and Taylor (1976).

0.95 and 1.05. As the effect of Pb loss and presence of possible measured inclusions with radiogenic Pb on the concordant data are unknown, normal age calculations over concordia age calculations has been preferred. Concordia age calculations generally result in similar ages with higher MSWD values. Thirteen zircon grains from sample E239 define an

intercept age of 434 ± 9 (2σ , MSWD = 1.3; Fig. 11b). Likewise, fifteen zircon grains from sample E241 yielded an intercept age of 439 ± 3 Ma (2σ , MSWD = 1.0; Fig. 11d). Eleven concordant zircon grains from sample E36 results in an intercept age of 446 ± 10 Ma (2σ , MSWD = 1.06). On the other hand, the weighted mean

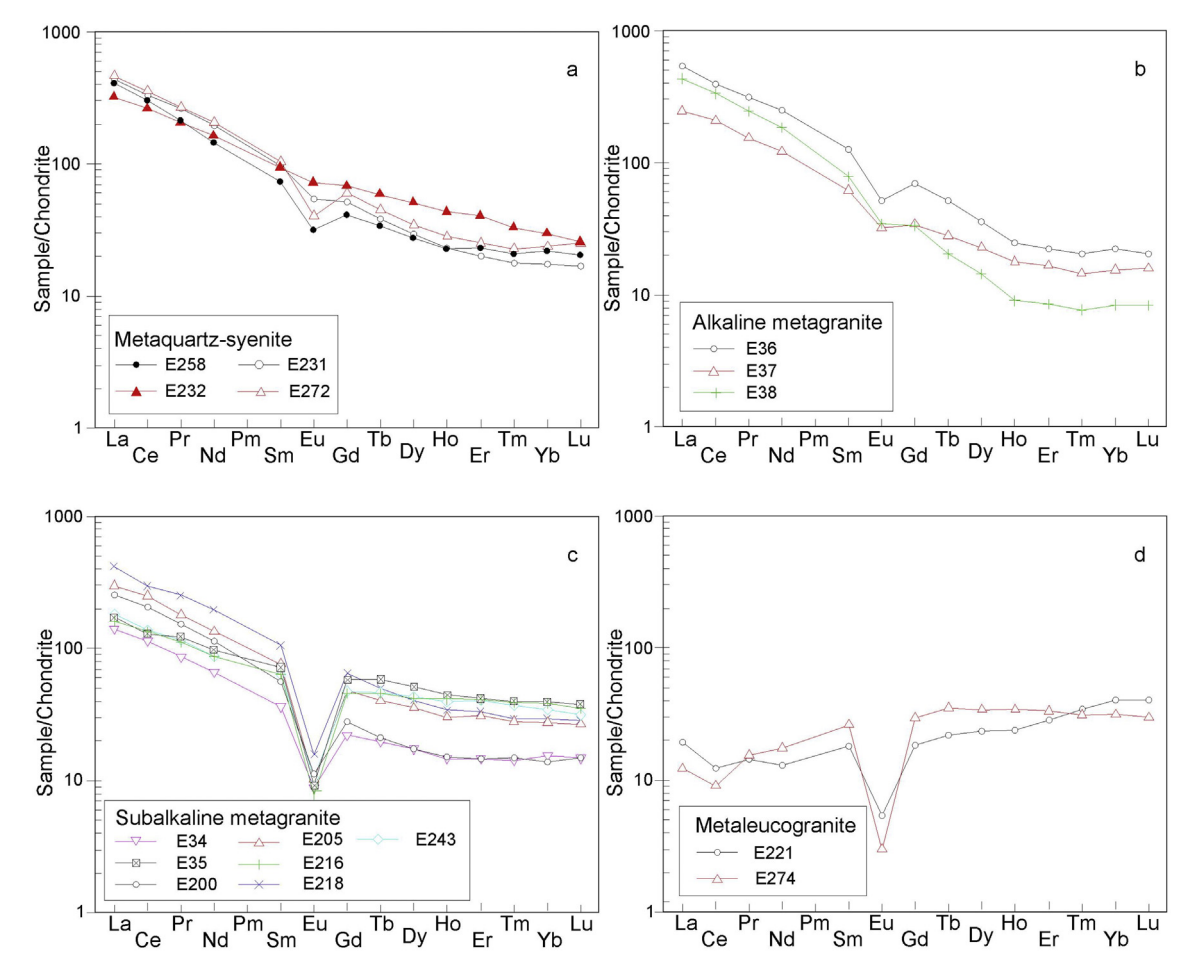


Fig. 8. Chondrite-normalized rare earth element diagrams of the different rock types from the Taşlıçay-Diyadin metaigneous complex. Normalizing values were taken from Boynton (1984).

²⁰⁶Pb/²³⁸U ages are 430 + 8/-4 Ma (2σ) in sample E239, 440 + 2/-5 Ma (2σ) in sample E241 and 423 + 8/-6 Ma (2σ) in sample E36 (not shown). In samples E36 and E241, there is only one zircon grain in each of the samples with ²⁰⁶Pb/²³⁸U age values of 474 \pm 12 and 469 \pm 10 Ma (2σ), respectively, which are interpreted as inherited grains (Figs. 11c, e).

Based on the textural and geochemical features of the zircons, the obtained age values are interpreted as the ages of igneous crystallization. Given the range of uncertainties caused by partial Pb loss and inclusions with radiogenic Pb, the age data indicate that the A-type magmatism has occurred at 430–440 Ma (Silurian).

7. Hafnium and oxygen isotopic compositions of zircon

The zircons from samples E36 and E241 display similar hafnium isotopic compositions (Fig. 12a-b; Table A3). The initial ϵ Hf values of the zircons from sample E36, calculated to 440 Ma, range from 0.14 to 4.46 with a median of 2.59 \pm 1.14 (2 σ), and those from sample E241 range from 0.72 to 4.93 with a median of 2.30 \pm 1.29 (2 σ). The Hf isotope model ages, calculated to depleted mantle, range from 0.85 to 1.03 Ga (average 0.93 \pm 0.05 Ga, 2 σ). The zircons from sample E36 have δ^{18} O values ranging from 5.41 to 7.32% with a median of 6.50 \pm 0.48% (Fig. 12c; Table A4). δ^{18} O values of the mantle derived magmas are 5.3 \pm 0.6% (Valley et al., 1994). Thus, the zircon δ^{18} O values are slightly higher than those of the mantle derived magmas.

These positive initial ϵ Hf values of the igneous zircons conclusively point mainly to juvenile nature of the anorogenic ferroan quartz syenitic to granitic magmatism. The slightly higher zircon δ^{18} O values than those of the mantle suggest that slightly old-crustal material could have been assimilated.

8. Discussion

8.1. Zirconium saturation temperatures

Magma temperatures are estimated using the formulation of Watson and Harrison (1983) which has been revisited by Boehnke et al. (2013) and Gervasoni et al. (2016). Zirconium saturation is related to magma composition and temperature, while water content in the magma and pressure have seemingly no effect on the zirconium saturation in the melt.

The Zr concentrations in the investigated samples of the Taşlıçay-Diyadin metaintrusive complex range from 402 to 1179 $\mu g/g$ (Table 1). The temperatures calculated from Watson and Harrison (1983)'s formulation range from 854 to 993 °C. Temperatures obtained from the models of Boehnke et al. (2013) and Gervasoni et al. (2016) are slightly lower, 791–996 and 747–993 °C, respectively. The zirconium concentrations do not show any apparent linear relationship versus SiO_2 abundances on the Harker diagrams (Fig. 7). As granites undergo fractionation, zirconium concentration decreases. However, zircon was not a fractionating phase during the course of crystallization in the

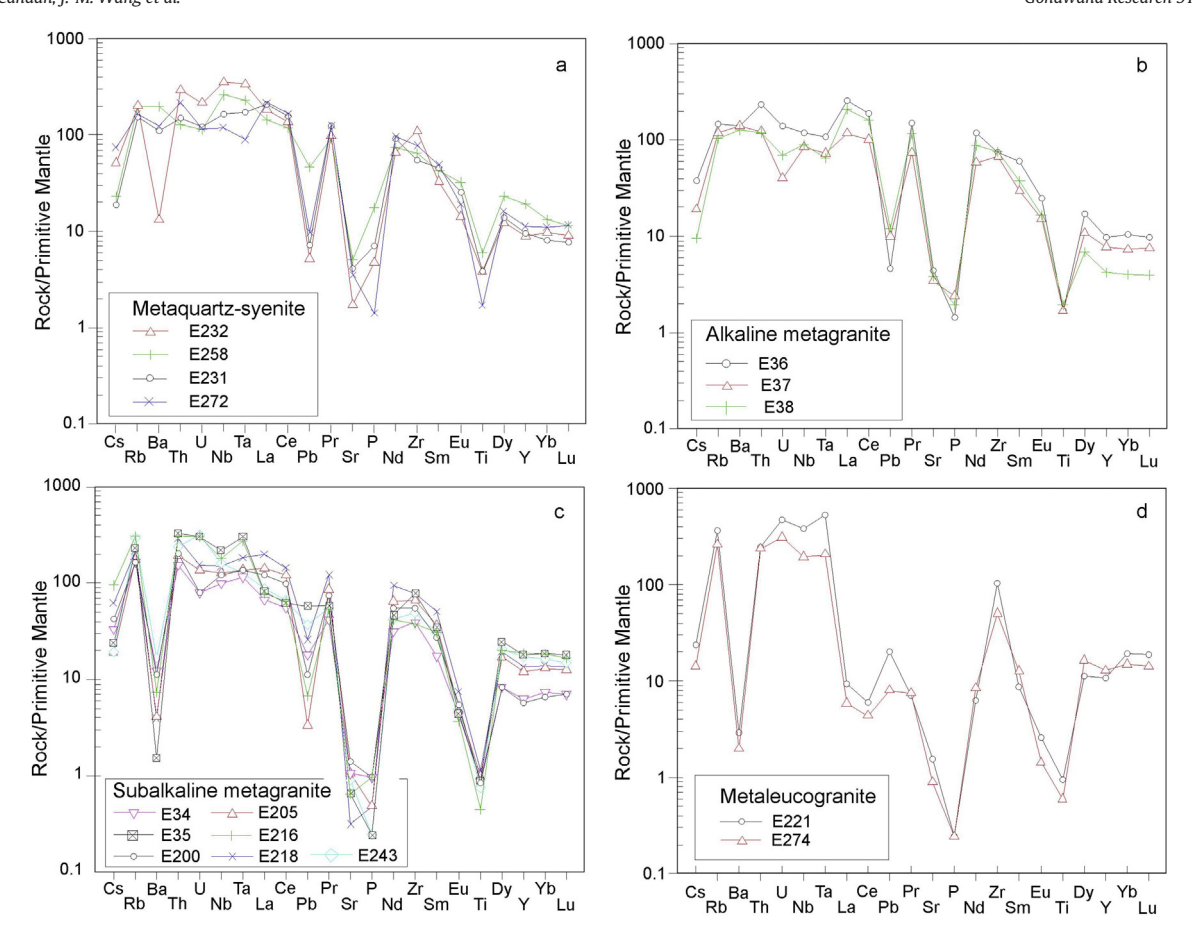


Fig. 9. Multielement variation diagrams of the different rock types from the Taşlıçay-Diyadin metaigneous complex. Normalizing values of primitive mantle and sequence of elements are from Sun and McDonough (1989).

Taşlıçay-Diyadin metaigneous complex. Only one inherited zircon grain out of 30 analyses was found in two samples (Fig. Table A2). Thus, significant amount of zircon inheritance can be ruled out.

The Taşlıçay-Diyadin metaintrusive complex formed from the high-temperature magmas with temperatures of 850–990 °C, implying significant heat input from mantle to crust. The obtained temperatures are similar to those calculated in A-type granites (Loiselle and Wones, 1979; Turner et al., 1992; King et al., 1997, 2001), and significantly higher than those normally for I- and S-type granites (e.g. Topuz and Okay, 2017; Topuz et al., 2019).

8.2. Source of A-type magmas, assimilation and crystal fractionation

Initial ϵ Hf and δ^{18} O values of the igneous zircons from the quartz metasyenite and –granite can be used to trace the source of the magmas. The initial ϵ Hf values of the igneous zircons (2.59 \pm 1.44 and 2.30 \pm 1.29; Figs. 12a-b; Table A3) point to juvenile nature of the magmas, and rules out derivation from crustal sources. On the other hand, the δ^{18} O values of the zircons are slightly higher (δ^{18} O = 6.58 \pm 0.48‰) than those of the mantle melts (5.3 \pm 0.6‰; Valley et al., 1994). This can be explained by assimilation of a small amount of high-silica crustal material. Given the elevated magma temperatures, 850–990 °C, this is probable. This is also in line with the presence of two inherited zircon grains with ages of ~470 Ma in samples E36 and E241 (Fig. 11; Table A2). As we do not have any constraint on the isotopic composition of the assimilated material, the exact amount of assimilated material is difficult to quantify. To sum up, the melts of the

Taşlıçay-Diyadin metaintrusive complex represent high-temperature mantle melts with minor crustal contamination.

Y/Nb ratio is considered as an important chemical index in distinguishing A₁ and A₂ granites with a border value of 1.2 (Eby, 1990) (Figs. 6c, 13). Y/Nb ratios lower than 1.2 are characteristic of A₁ granites. All the samples from the Taşlıçay-Diyadin complex have Y/Nb ratios ranging from 0.17 to 0.70. In terms of Y/Nb vs. Ce/Nb and Y/Nb vs. Yb/Ta, the samples resemble ocean-island basalts. The fundamental question here is whether these elemental ratios are influenced by the processes such as mineral fractionation, magma mixing and crustal assimilation. Both Ta and Nb show negative correction with increasing silica in metaquartz-syenite and alkaline metagranite, and form cluster at subalkaline metagranites and metaleucogranites. Albeit not so obvious, similar trends are shown by Y and Yb (not shown). This state requires fractionation of Nb- and Ta-bearing phase(s) in metaquartz-syenite and alkaline metagranite. As all these elements behave in the same way, it is improbable that their ratios are changed during the mineral fractionation. Thus, these rocks are direct fractionation products of the ocean island like basaltic magmas, whereby crustal contamination or mixing with crustal melts were insignificant.

The metaquartz-syenite and alkaline metagranite represent distinct magma pulse, and are not related to subalkaline granites by crystal fractionation. Several features of the REE patterns of the metaquartz-syenite and alkaline metagranite such as (i) highly fractionated nature of REE patterns ((La/Yb) $_{\rm cn} \sim 11-51$; (Gd/Yb) $_{\rm cn} \sim 2-4$; Table 1), (ii) negative Eu anomaly (Eu/Eu* $\sim 0.51-0.90$) and (iii) concave upward form of the middle to heavy rare earth elements (e.g. Romick et al., 1992) (Figs. 8a-b) suggest a fractionating

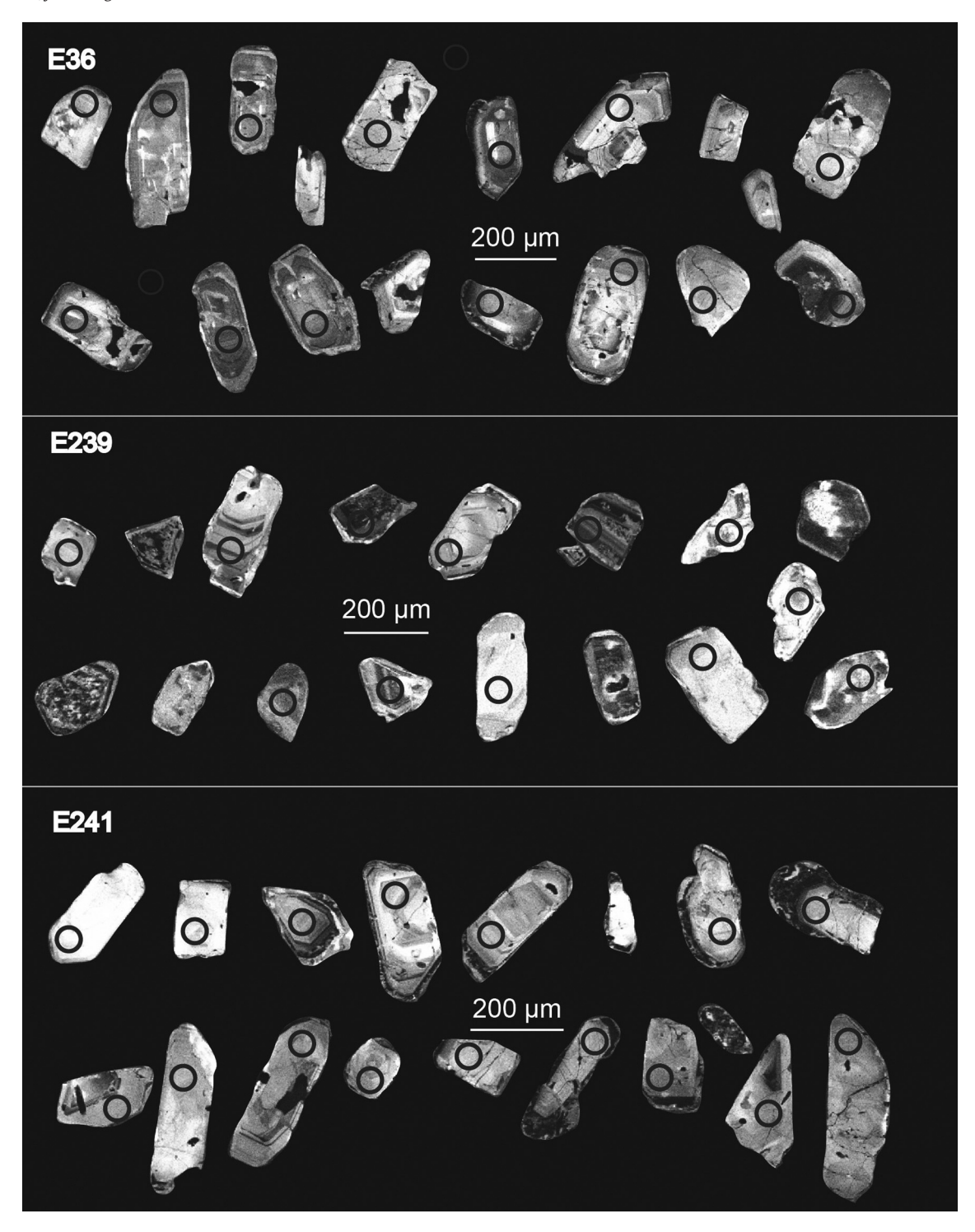


Fig. 10. Cathodoluminescence images of the dated zircons from samples E36B, E237 and E241.

mineral assemblage of garnet, plagioclase and amphibole. On the other hand, the subalkaline granites have less steep REE patterns ((La/Yb)_{cn} ~ 4–18; (Gd/Yb)_{cn} ~ 1–2) and much more pronounced negative Eu anomalies (Eu/Eu* ~ 0.14–0.31) (Fig. 8c). Likewise, negative Ba anomaly is nearly absent in metaquartz-syenite and alkaline metagranite, and becomes obvious in subalkaline metagranite and metaleucogranite (Fig. 9). This suggests significant amount of plagioclase fractionation without significant involvement of garnet. Thus, it is probable that the subalkaline granite underwent a second stage of fractionation in a shallower magma chamber relative to the

metaquartz-syenite and alkaline metagranite. The decrease in the steepness of the REE patterns can be explained by the fractionation of a mineral which preferentially incorporate LREE with respect to the HREEs such plagioclase, allanite, bastnesite and fluorbritholite. Decrease of ${\rm TiO}_2$ with increasing silica and presence of the steadily increasing negative Ti anomaly on spider diagrams from quartz syenite to alkaline granite (Figs. 7 and 9a-b) can be explained by fractionation of Fe–Ti oxide and amphibole. Likewise, steadily decrease of ${\rm P}_2{\rm O}_5$ (not shown) and negative anomaly of P on spider diagrams suggest apatite fractionation.

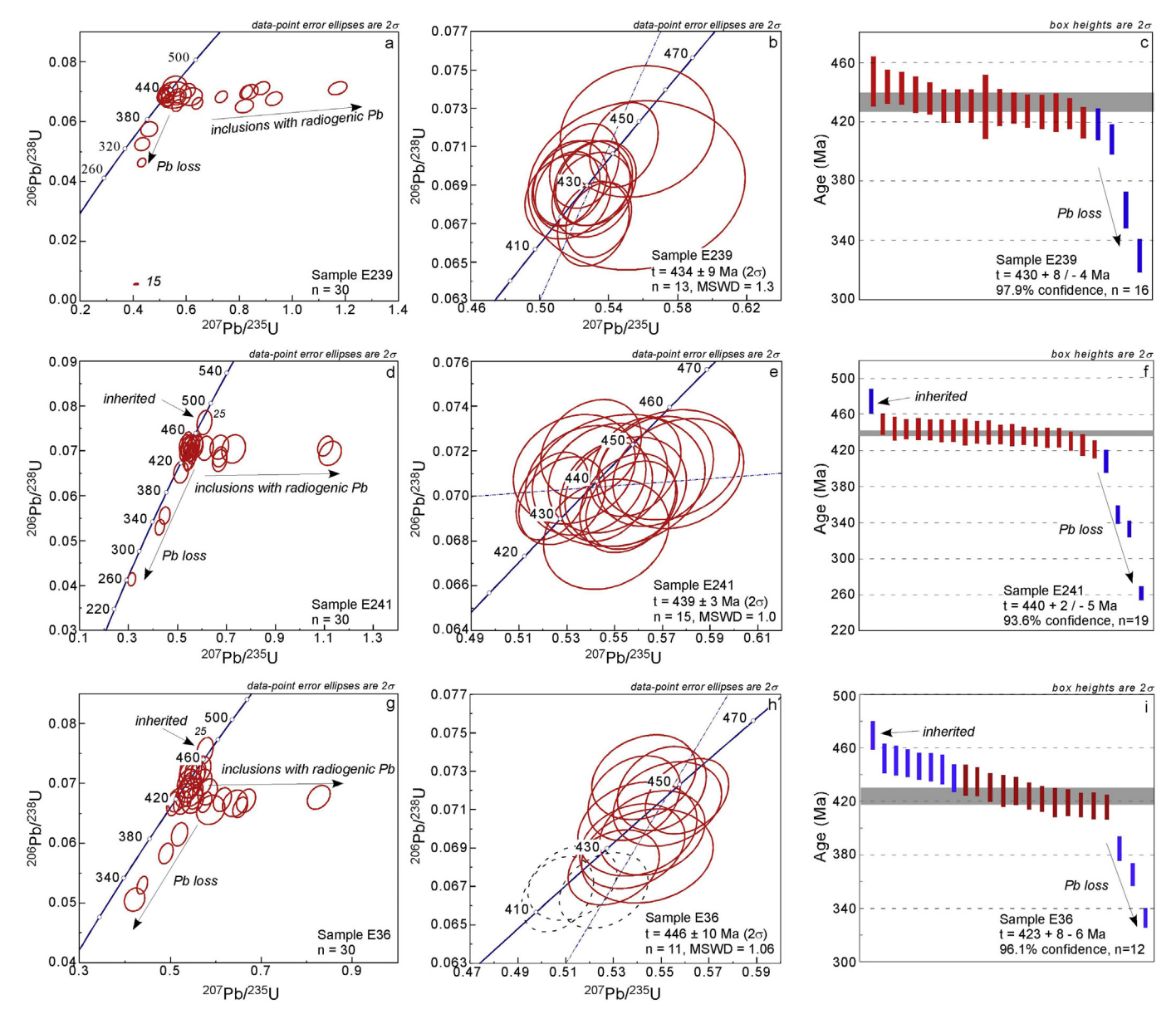


Fig. 11. U-Pb concordia diagrams for the dated zircons from samples E36B, E237 and E241. Age calculations have been performed by Isoplot 4.15 (Ludwig, 2003).

8.3. Geodynamic implications

As pointed out earlier, igneous activity during Paleozoic time is rare and sporadic in both the Anatolide-Tauride and the NW Iranian blocks (Fig. 1). The igneous rocks documented so far in the Anatolide-Tauride block include Middle to Late Ordovician granite and rhyolite, Late Carboniferous granites and Permo-Triassic basalt, trachyandesite, dasite and rhyolite (Okay et al., 2008a; Özbey et al., 2013a, 2013b; Candan et al., 2016; Akal et al., 2012). In this respect, the Taşlıçay-Diyadin metaquartz-syenite to -granite represent the first example of Silurian magmatism in the Anatolide-Tauride block. The provenance studies on the Carboniferous and Triassic clastic rocks from the Anatolide-Tauride block have revealed the sporadic presence of detrital zircons with Ordovician, Silurian, Devonian and Carboniferous Permian igneous crystallization ages (Okay et al., 2008a; Ustaomer et al., 2019; Löwen et al., 2020), suggesting the sporadic presence of magmatism throughout the Paleozoic. In comparison, Paleozoic anorogenic magmatism has been much better documented in the NW Iranian block (Ordovician basic and acidic magmatism Shahsavari Alavijeh et al., 2018; Moghadam et al., 2017; Moghadam et al., 2018; Silurian anorogenic al-kaline mafic rocks Vesali et al., 2020; Devonian A-type granite Abdulzahra et al., 2016; Mohammadi et al., 2020; Carboniferous A-type granite and gabbro Moghadam et al., 2015, Mohammadi et al., 2020; Permian A-type granite Alirezaei and Hassanzadeh, 2012). This suggests that the NW Iranian block was site of anorogenic magmatism throughout the Paleozoic.

It is commonly accepted that the Anatolide-Tauride and NW Iranian blocks were a passive continental margins throughout the Paleozoic, and was located at the norther margin of Gondwana, and it detached from the Gondwana first during the Permian-Early Triassic (e.g. Şengör and Yılmaz, 1981; Şengör, 1990). This interpretation is based on the fact that (i) the Paleozoic rocks in the non-metamorphosed parts of the Anatolide-Tauride block are made up of carbonate and clastic sedimentary rocks extending in age from Cambrian to Triassic with local presence of Silurian and Permian unconformities (Özgül, 1976; Göncüoğlu and Kozlu, 2000; Monod et al., 2003), (ii) Paleozoic igneous rocks are minor and sporadic (Okay et al., 2008a; Özbey et al., 2013a, 2013b; Candan et al., 2016; Akal et al., 2012), (iii) the absence of any

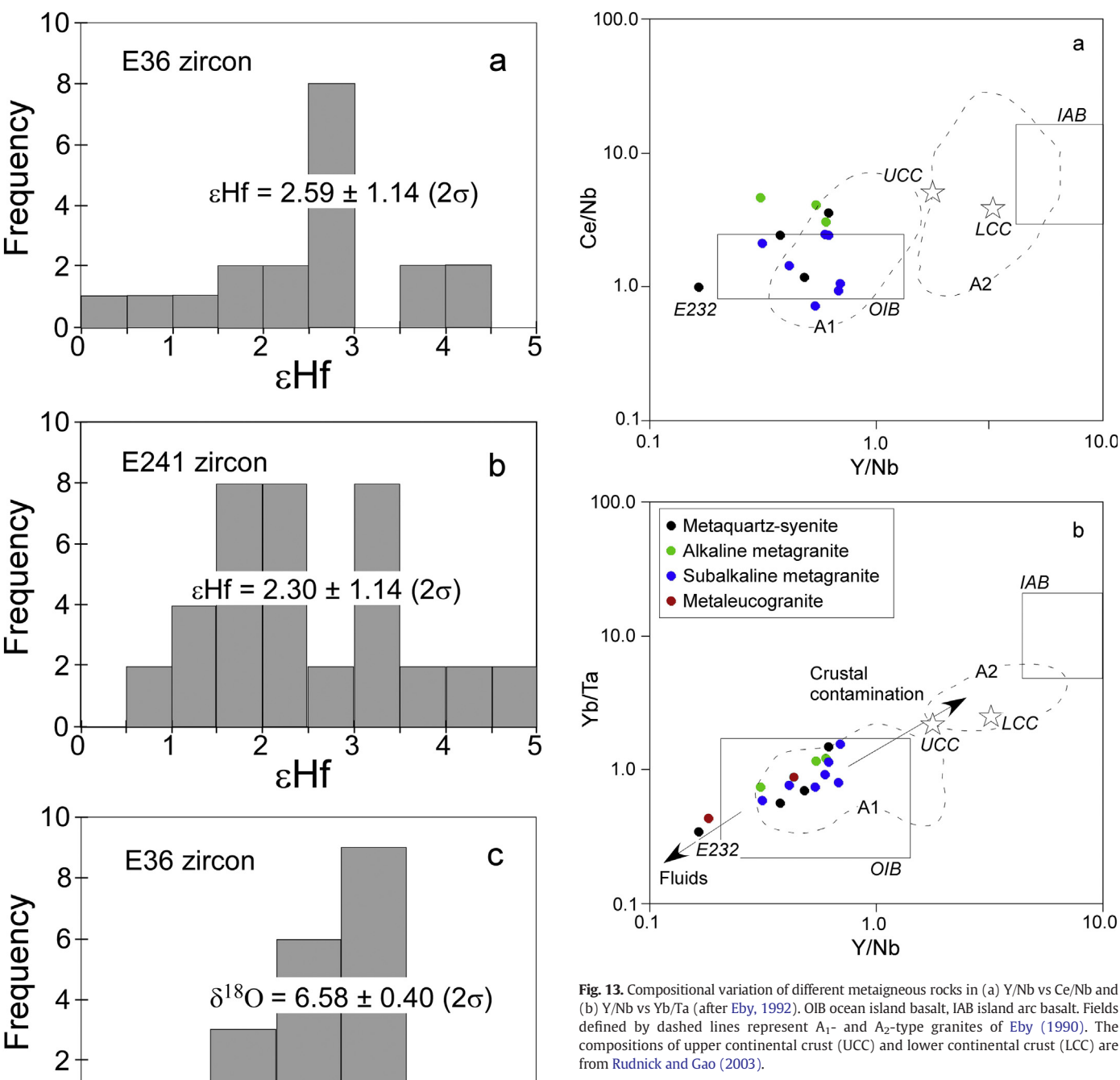


Fig. 12. Histograms showing ϵ Hf(440 Ma) values of zircons from (a) samples E36B and (b) E241), (c) Histogram of δ^{18} O values of the igneous zircons from sample E36.

 $^6_{
m 5^{18}O}$

0

Paleozoic accretionary complexes along the northern margin of Anatolide-Tauide block, apart from the Carboniferous ones (e.g. Ustaomer et al., 2019; Löwen et al., 2020), and (iv) ages of the deep marine sedimentary rocks range from Triasic to Late Cretaceous (e.g. Uzunçimen et al., 2011). However, the sporadic Carboniferous and Permo-Triassic magmatic rocks were interpreted to have formed in a subduction-related environment beneath the northern margin of Gondwana (Akal et al., 2012; Candan et al., 2016; Löwen et al., 2020), what is outside the scope of this study.

(b) Y/Nb vs Yb/Ta (after Eby, 1992). OIB ocean island basalt, IAB island arc basalt. Fields defined by dashed lines represent A₁- and A₂-type granites of Eby (1990). The compositions of upper continental crust (UCC) and lower continental crust (LCC) are

The Lower to Middle Ordovician sedimentary rocks in both the Anatolide-Tauride block and the Arabian platform are represented by shales grading upward into sandstone (the Seydisehir Formation). This formation is unconformably overlain by Middle to Upper Ordovician sequence starting with a thin layer of limestone and grade upward into siltstone (Monod et al., 2003; Ghienne et al., 2010). Several features such as (i) the presence of unconformity between Middle and Upper Ordovician, (ii) regression associated with gravity-driven facies, and (iii) reworking of palynomorph assemblages were interpreted in terms of rifting/extensional setting as of Late Ordovician. This extensional setting went on during Silurian time. Therefore, Late Ordovician to Silurian magmatism in the Anatolide-Tauride block is probably rifting-related. Likewise, Late Ordovician-Silurian magmatism is of anorogenic nature in the Gondwanian continental blocks such as Sakarya Zone, the Caucasus and Rhodope-Strandja zone, all of which are regarded part of the Armorica terrain assemblage (e.g. Topuz et al., 2020). Hence, Topuz et al.

8

Late Ordovician-Silurian

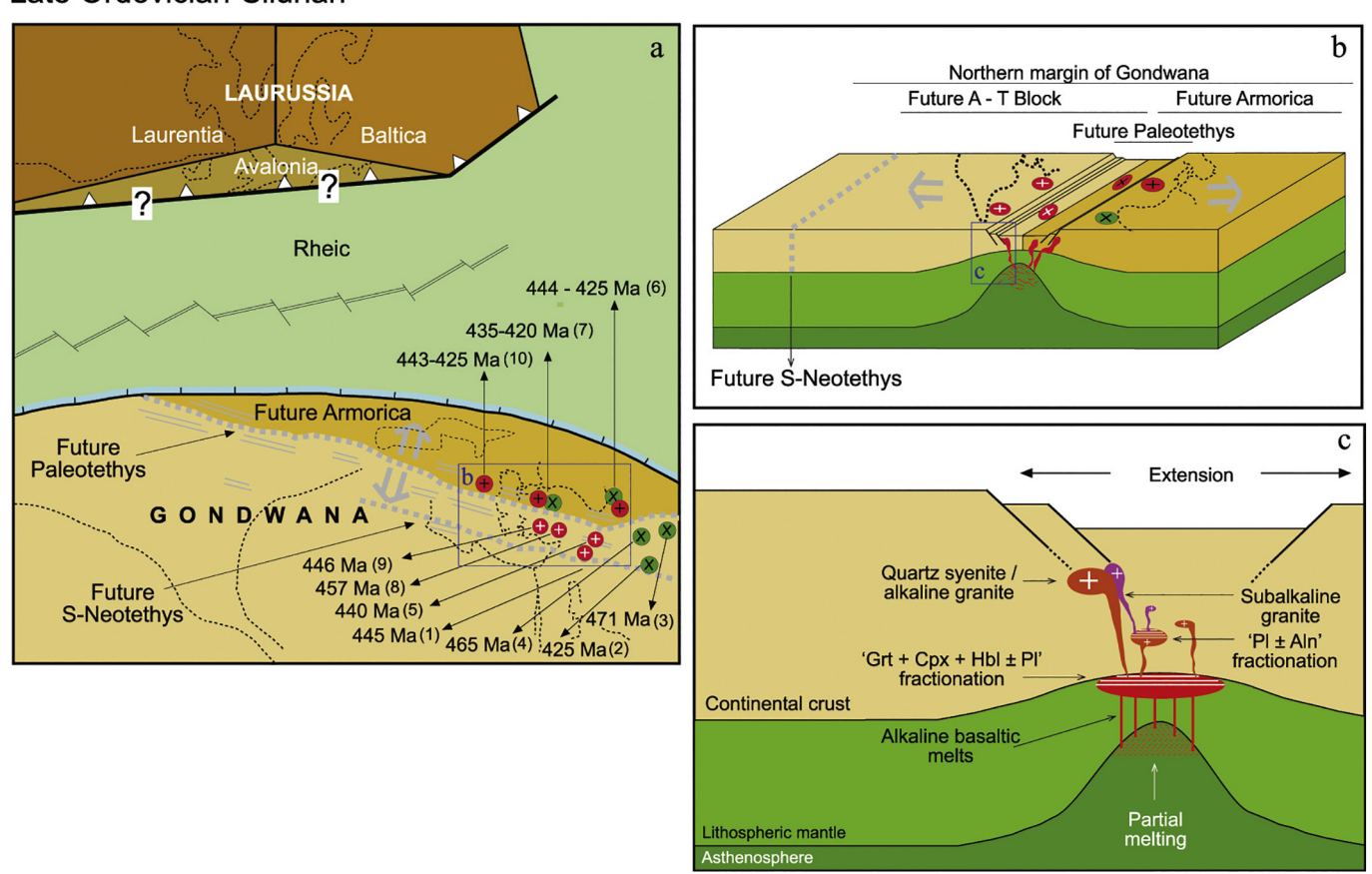


Fig. 14. Schematic illustrations showing formation of the A-type quartz syenite to granite in the Anatolide-Tauride block. a During Late Ordovian, northern margin of Gonwana undergoing extension and rifting, leading to the opining of Paleo-Tethys. Consequently, anorogenic basic to acidic magmatism developed in the continental domains to the south and north of Paleo-Tethys. The numbers in parentheses represent references, and are the same as in Fig. 1. b Schematic block diagram showing the opening of Paleo-Tethys and associated magmatism, and c Schematic cross-section showing formation of the Taşlıçay-Diyadin metaquartz syenite to metagranite complex. Partial melting of the rising asthenosphere leads to formation of alkaline basic magmas. These alkaline-basic magmas are subjected to the fractionation of garnet + amphibole ± plagioclase in a deep-seated magma chamber. The remaining melts of probably syenitic composition rose and emplaced into a shallow magma chamber. On the other hand, the parental melts of subalkaline granite underwent fractionation of plagioclase and allanite in an additional crustal magma chamber, before emplacing into the shallow magma chamber. (For interpretation of the references to color in this figure legend, the reader is referred to the web version of this article.)

(2020) suggested that the Silurian extensional setting led to the detachment of the Armorican terrane assemblage from Gondwana, and thus the opening of the Paleo-Tethys.

For the genesis of the Taşlıçay-Diyadin igneous complex we suggest the following evolutionary history. The northern margin of Gondwana was undergoing extension during Late Ordovician to Silurian time in response to the detachment of the Armorica (e.g. the Sakarya zone) (Fig. 14). This extension/rifting led to crustal thinning associated with anorogenic magmatism in both northern margin of Gondwana and Armorica (the Sakarya zone). Decompressional melting of the incompatible element enriched mantle sources due to the rifting resulted in the genesis of alkaline ocean island basalt-like melts. As ocean island basaltic melts are ultimately related to the melting in asthenosphere (e.g. Humphreys and Niu, 2009; Niu et al., 2012), we tentatively suggest that the melting was initiated in asthenosphere. These alkaline ocean island basaltic melts underwent fractional crystallization involving garnet, clinopyroxene, amphibole and \pm plagioclase at a relatively deep-seated magma chamber. The fractionated melts rose to the shallow-level magma chamber. Fractional crystallization and solidification of this melts resulted in the formation of quartz syenite, and alkaline granite. On the other hand, formation of subalkaline granite requires a second stage of mineral fractionation

at middle crustal levels whereby plagioclase \pm allanite fractionation played major role. Therefore, we infer that the melts of the subalkaline granite were emplaced at the middle crustal magma chamber where plagioclase and allanite fractionated before emplacement at the final shallow magma chamber.

9. Conclusions

The Taşlıçay-Diyadin metaintrusive complex in the East Anatolian plateau comprises rock types including metaquartz-syenite, alkaline metagranite, subalkaline metagranite and metaleucogranite. U-Pb zircon dating consistently point to emplacement at 430–440 Ma (Silurian) into a sedimentary sequence of Late Neoproterozoic to Early Paleozoic age. All the rock types are geochemically characterized by their elevated Na₂O, K₂O, high-field strength and rare earth element abundances and low abundances of CaO, MgO and Sr, similar to A-type syenites to granites. The rock types range from peralkaline to metaluminous to peraluminous compositions. Metaquartz-syenite and alkaline metagranite are not related to subalkaline metagranite and metaleucogranite by mineral fractionation, and represent distinct magma pulses from similar source with different degree of fractionation. The intrusive complex has formed from high-temperature

magmas with temperatures of 850–990 °C. The initial ϵ Hf values of zircons (2.30–2.60) point to the juvenile nature of the magmas of the original quartz syenite to granite. Despite elevated magma temperatures, the assimilation of the crustal material or mixing with crustal melts were insignificant. Anorogenic magmatism of Late Ordovician to Silurian age are widespread in the Anatolide-Tauride block and NW Iranian block which were detached from Gondwana first during Permo-Triassic times and Sakarya zone which detached from Gondwana during Silurian time in the Tethyan belt. These data together with those from literature are interpreted to have formed during a rifting event, leading to the detachment of Armorica from the northern margin of Gondwana.

Author statement

Gültekin Topuz, Osman Candan and Ali Yılmaz have mapped the area, and sampled the intrusion. Jia-Min Wang, Qui-Li Li and Fu-Yuan Wu have contributed during the analytical work such as dating and Hf and O-isotopy of zircons. The manuscript has been written by Gültekin Topuz and Osman Candan. The end version of the manuscript has been read by all coauthors. In line with the ideas of all the coauthors the manuscript has been modified. All the coauthors read the paper, and agree with the presented ideas.

Declaration of Competing Interest

The authors declare that they have no known competing financial interests or personal relationships that could have appeared to influence the work reported in this paper.

Acknowledgements

We have grateful to Aral I. Okay for the fruitful discussions on the Paleozoic evolution of the Anatolide-Tauride block. We gratefully acknowledge helpful and constructive reviews by Hadi Shafaii Moghadam and an anonymous reviewer. Financial support for this study has been provided by from the Scientific and Technological Research Council of Turkey (TÜBİTAK, research grant #114Y226), the Istanbul Technical University (research grant #39140) and the National Natural Science Foundation of China (research grants #41888101 and #41972065). We thank Mutlu Özkan for helps during mineral separation, and Evren Çubukçu, Erkan Aydar and Axel Sjöqvist for helps during the cathodoluminescence and scanning electron microscope documentation of zircons.

Appendix A. Supplementary data

Supplementary data to this article can be found online at https://doi.org/10.1016/j.gr.2020.12.005.

References

- Abdulzahra, I.K., Hadi, A., Asahara, Y., Azizi, H., Yamamoto, K., 2016. Zircon U–Pb ages and geochemistry of devonian a-type granites in the iraqi zagros suture zone (Damamna area): new evidence for magmatic activity related to the Hercynian orogeny. Lithos 264, 360–374
- Açlan, M., Duruk, H.İ., 2018. Geochemistry, zircon U-Pb geochronology, and tectonic setting of the Taşlıçay granitoids, Eastern Anatolia, Turkey. Arab. J. Geosci. 11, 336.
- Açlan, M., Turgut, I.K., 2020. Zircon U–Pb ages and geochemistry of granitoid from the southwest part of the Taşlıçay batholith: implications for neotethyan closure in Eastern Anatolia, Turkey. J. Earth Syst. Sci. 129, 1–18.
- Ague, J.J., 2017. Element mobility during regional metamorphism in crustal and subduction zone environments with a focus on the rare earth elements (REE). Am. Mineral. 102, 1796–1821.

- Akal, C., Candan, O., Koralay, O.E., Oberhänsli, R., Chen, F., Prelević, D., 2012. Early Triassic potassic volcanism in the Afyon Zone of the Anatolides/Turkey: implications for the rifting of the Neo-Tethys. Int. J. Earth Sci. 101, 177–194.
- Alirezaei, S., Hassanzadeh, J., 2012. Geochemistry and zircon geochronology of the Permian A-type Hasanrobat granite, Sanandaj–Sirjan belt: a new record of the Gondwana break-up in Iran. Lithos 151, 122–134.
- Antić, M., Peytcheva, I., von Quadt, A., Kounov, A., Trivić, B., Serafimovski, T., Tasev, G., Gerdjikov, I., Wetzel, A., 2016. Pre-Alpine evolution of a segment of the North-Gondwanan margin: geochronological and geochemical evidence from the central Serbo-Macedonian Massif. Gondwana Res. 36, 523–544.
- Boehnke, P., Watson, E.B., Trail, D., Harrison, T.M., Schmitt, A.K., 2013. Zircon saturation rerevisited. Chem. Geol. 351, 324–334.
- Bonin, B., 2007. A-type granites and related rocks: evolution of a concept, problems and prospects. Lithos 97, 1–29.
- Boynton, W.V., 1984. Cosmochemistry of the rare earth elements: Meteorite studies. In: Henderson, P. (Ed.), Rare Earth Element Geochemistry. Elsevier, Amsterdam, pp. 63–114.
- Candan, O., Çetinkaplan, M., Oberhänsli, R., Rimmelé, G., Akal, C., 2005. Alpine high-P/low-T metamorphism of the Afyon Zone and implications for the metamorphic evolution of Western Anatolia, Turkey. Lithos 84, 102–124.
- Candan, O., Akal, C., Koralay, O.E., Okay, A.I., Oberhänsli, R., Prelević, D., Mertz-Kraus, R., 2016. Carboniferous granites on the northern margin of Gondwana, Anatolide–Tauride Block, Turkey–evidence for southward subduction of Paleotethys. Tectonophysics 683, 349–366.
- Eby, G.N., 1990. The A-type granitoids: a review of their occurrence and chemical characteristics and speculations on their petrogenesis. Lithos 26, 115–134.
- Eby, G.N., 1992. Chemical subdivision of the A-type granitoids: petrogenetic and tectonic implications. Geology 20, 641–644.
- Frost, B.R., Arculus, R.J., Barnes, C.G., Collins, W.J., Ellis, D.J., Frost, C.D., 2001. A geochemical classification of granitic rock suites. J. Petrol. 42, 2033–2048.
- Frost, C.D., Frost, B.R., 1997. Reduced rapakivi-type granites: the tholeite connection. Geology 25, 647–650
- Frost, C.D., Frost, B.R., 2011. On ferroan (A-type) granites: their compositional variability and modes of origin. J. Petrol. 52, 39–53.
- Frost, C.D., Frost, B.R., Chamberlain, K.R., Edwards, B.R., 1999. Petrogenesis of the 1.43 Ga Sherman batholith, SE Wyoming, USA: a reduced, rapakivi-type anorogenic granite. J. Petrol. 40, 1771–1802.
- Gervasoni, F., Klemme, S., Rocha-Júnior, E.R., Berndt, J., 2016. Zircon saturation in silicate melts: a new and improved model for aluminous and alkaline melts. Contrib. Mineral. Petrol. 171 (3), 21.
- Ghienne, J.F., Monod, O., Kozlu, H., Dean, W.T., 2010. Cambrian–Ordovician depositional sequences in the Middle East: a perspective from Turkey. Earth Sci. Rev. 101, 101–146
- Gill, R., 2011. Igneous Rocks and Processes: A Practical Guide. John Wiley and Sons, Oxford, p. 428.
- Göncüoğlu, M.C., Kozlu, H., 2000. Early Paleozoic evolution of the NW Gondwanaland: data from southern Turkey and surrounding regions. Gondwana Res. 3, 315–324.
- Göncüoğlu, M.C., Turhan, N., Tekin, U.K., 2003. Evidence for the Triassic rifting and opening of the Neotethyan Izmir-Ankara Ocean and discussion on the presence of Cimmerian events at the northern edge of the Tauride-Anatolide Platform, Turkey. Boll. Soc. Geol. Ital. 2, 203–212.
- Humphreys, E.R., Niu, Y., 2009. On the composition of ocean island basalts (OIB): the effects of lithospheric thickness variation and mantle metasomatism. Lithos 112, 118–136.
- Irvine, T.N., Baragar, W.R.A., 1971. A guide to chemical classification of the common volcanic rocks. Can. J. Earth Sci. 8, 523–548.
- King, P.L., White, A.J.R., Chappell, B.W., Allen, C.M., 1997. Characterization and origin of aluminous A-type granites from the Lachlan Fold Belt, southeastern Australia. J. Petrol. 38, 371–391.
- King, P.L., Chappell, B.W., Allen, C.M., White, A.J.R., 2001. Are A-type granites the high-temperature felsic granites? Evidence from fractionated granites of the Wangrah Suite. Aust. J. Earth Sci. 48, 501–514.
- Loiselle, M.C., Wones, D.R., 1979. Characteristics of anorogenic granites. Geol. Soc. Am. Abstr. Programs 11, 468.
- Löwen, K., Meinhold, G., Arslan, A., Güngör, T., Berndt, J., 2020. Evolution of the Palaeotethys in the Eastern Mediterranean: a multi-method approach to unravel the age, provenance and tectonic setting of the Upper Palaeozoic Konya complex and its Mesozoic cover sequence (south-Central Turkey). Int. Geol. Rev. 62, 389–414.
- Ludwig, K.R., 2003. Isoplot/Ex 3.00. A Geochronological toolkit for Microsoft Excel. Berkely Geochronological Center Special Publication No. 4.
- Middlemost, E.A.K., 1994. Naming materials in the magma/igneous rock system. Earth Sci. Rev. 37, 215–224.
- Moghadam, F.R., Masoudi, F., Corfu, F., Homam, S.M., 2018. Ordovician mafic magmatism in an Ediacaran arc complex, Sibak, northeastern Iran: the eastern tip of the Rheic Ocean. Can. J. Earth Sci. 55, 1173–1182.
- Moghadam, H.S., Li, X.H., Ling, X.X., Stern, R.J., Santos, J.F., Meinhold, G., ... Shahabi, S., 2015. Petrogenesis and tectonic implications of Late carboniferous A-type granites and gabbronorites in NW Iran: geochronological and geochemical constraints. Lithos 212, 266–279.
- Moghadam, H.S., Li, X.H., Griffin, W.L., Stern, R.J., Thomsen, T.B., Meinhold, G., ... O'Reilly, S.Y., 2017. Early paleozoic tectonic reconstruction of Iran: tales from detrital zircon geochronology. Lithos 268, 87–101.

- Mohammadi, A., Moazzen, M., Lechmann, A., Laurent, O., 2020. Zircon U-Pb geochronology and geochemistry of Late Devonian-Carboniferous granitoids in NW Iran: implications for the opening of Paleo-Tethys. Int. Geol. Rev. 1–18.
- Monod, O., Kozlu, H., Ghienne, J.F., Dean, W.T., Günay, Y., Herisse, A.L., Paris, F., Robardet, M., 2003. Late Ordovician glaciation in southern Turkey. Terra Nova 15, 249–257.
- Niu, Y.L., Wilson, M., Humphreys, E.R., O'Hara, M.J., 2012. A trace element perspective on the source of ocean island basalts (OIB) and fate of subducted ocean crust (SOC) and mantle lithosphere (SML). Episodes 35, 310–327.
- Okay, A.I., 2000. Was the late Triassic orogeny in Turkey caused by the collision of an oceanic plateau? Geol. Soc. Lond., Spec. Publ. 173, 25–41.
- Okay, A.I., Topuz, G., 2017. Variscan orogeny in the Black Sea region. Int. J. Earth Sci. 106, 569–592
- Okay, A.I., Satır, M., Shang, C.K., 2008a. Ordovician metagranitoid from the Anatolide-Tauride block, Northwest Turkey: geodynamic implications. Terra Nova 20, 280–288.
- Okay, A.I., Bozkurt, E., Satır, M., Yiğitbaş, E., Crowley, Q.G., Shang, C.K., 2008b. Defining the southern margin of Avalonia in the Pontides: geochronological data from the late Proterozoic and Ordovician granitoids from NW Turkey. Tectonophysics 461, 252-264.
- Özbey, Z., Ustaömer, T., Robertson, A.H.F., Ustaömer, P.A., 2013a. Tectonic significance of late Ordovician granitic magmatism and clastic sedimentation on the northern margin of Gondwana (Tavşanlı Zone, NW Turkey). J. Geol. Soc. Lond. 170, 159–173.
- Özbey, Z., Ustaömer, T., Robertson, A.H., 2013b. Mesozoic magmatic and sedimentary development of the Tavşanlı Zone (NW Turkey): implications for rifting, passive margin development and ocean crust emplacement. Geol. Soc. Lond., Spec. Publ. 372, 141–165
- Özgül, N., 1976. Some geological aspects of the Taurus orogenic belt (Turkey). Bull. Geol. Soc. Turk. 19, 65–78.
- Peccerillo, A., Taylor, S.R., 1976. Geochemistry of Eocene calc-alkaline volcanic rocks from the Kastamonu area, northern Turkey. Contrib. Mineral. Petrol. 58, 63–81.
- Polat, A., Hofmann, A.W., 2003. Alteration and geochemical patterns in the 3.7–3.8 Ga Isua greenstone belt, West Greenland. Precambrian Res. 126, 197–218.
- Pourteau, A., Sudo, M., Candan, O., Lanari, P., Vidal, O., Oberhänsli, R., 2013. Neotethys closure history of Anatolia: insights from 40Ar–39Ar geochronology and P–T estimation in high-pressure metasedimentary rocks. J. Metamorph. Geol. 31, 585–606.
- Rolland, Y., Hässig, M., Bruguier, O., Bosch, D., Mélis, R., Galoyan, G., Topuz, T., Sahakyan, L., Avagyan, A., 2020. The East Anatolia–Lesser Caucasus ophiolite: an exceptional case of large-scale obduction, synthesis of data and numerical modelling. Geosci. Front. 11, 83–108
- Romick, J.D., Kay, S.M., Kay, R.W., 1992. The influence of amphibole fractionation on the evolution of calc-alkaline andesite and dacite tephra from the central Aleutians, Alaska. Contrib. Mineral. Petrol. 112, 101–118.
- Rudnick, R.L., Gao, S., 2003. Composition of the continental crust. Crust 3, 1-64.
- Schmid, S.M., Bernoulli, D., Fügenschuh, B., Matenco, L., Schefer, S., Schuster, R., Tischler, M., Ustaszewski, K., 2008. The Alpine-Carpathian-Dinaridic orogenic system: correlation and evolution of tectonic units. Swiss J. Geosci. 101, 139–183.
- Schmidt, A., Pourteau, A., Candan, O., Oberhänsli, R., 2015. Lu–Hf geochronology on cmsized garnets using microsampling: New constraints on garnet growth rates and duration of metamorphism during continental collision (Menderes Massif, Turkey). Earth Planet. Sci. Lett. 432, 24–35.
- Şengör, A.M.C., 1990. A new model for the late Palaeozoic—Mesozoic tectonic evolution of Iran and implications for Oman. Geol. Soc. Lond., Spec. Publ. 49, 797–831.
- Şengör, A.M.C., Yılmaz, Y., 1981. Tethyan evolution of Turkey: a plate tectonic approach. Tectonophysics 75, 181–241.
- Shahsavari Alavijeh, B., Rashidnejad-Omran, N., Toksoy-Köksal, F., Chew, D., Szopa, K., Ghalamghash, J., Gaweda, A., 2018. Geochemistry and apatite U-Pb geochronology of alkaline gabbros from the Nodoushan plutonic complex, Sanandaj-Sirjan Zone, Central Iran: evidence for early Palaeozoic rifting of northern Gondwana. Geol. J. 54, 1902–1926
- Shand, S.J., 1943. Eruptive rocks. Their Genesis, Composition, Classification and their Relation to Ore Deposits, with a Chapter on Meteorite. Wiley, New York.
- Sherlock, S., Kelley, S., Inger, S., Harris, N., Okay, A., 1999. ⁴⁰Ar-³⁹Ar and Rb-Sr geochronology of high-pressure metamorphism and exhumation history of the Tavsanli Zone, NW Turkey. Contrib. Mineral. Petrol. 137, 46–58.
- Somin, M.L., 2011. Pre-Jurassic basement of the Greater Caucasus: brief overview. Turk. J. Earth Sci. 20, 545–610.

- Sun, S.-S., McDonough, W.F., 1989. Chemical and isotopic systematics of oceanic basalts: Implications for mantle composition and processes. In: Saunders, A.D., Norry, M.J. (Eds.), Magmatism in the Ocean Basins. Geological Society of London Special Publication vol. 42, pp. 313–345.
- Topuz, G., Okay, A.I., 2017. Late Eocene–early Oligocene two-mica granites in NW Turkey (the Uludağ Massif): water-fluxed melting products of a mafic metagreywacke. Lithos 268, 334–350
- Topuz, G., Altherr, R., Siebel, W., Schwarz, W.H., Zack, T., Hasözbek, A., Barth, M., Satır, M., Şen, C., 2010. Carboniferous high-potassium I-type granitoid magmatism in the Eastern Pontides: the Gümüşhane pluton (NE Turkey). Lithos 116, 92–110.
- Topuz, G., Göçmengil, G., Rolland, Y., Çelik, Ö.F., Zack, T., Schmitt, A.K., 2013. Jurassic accretionary complex and ophiolite from Northeast Turkey: no evidence for the Cimmerian continental ribbon. Geology 45, 255–258.
- Topuz, G., Candan, O., Zack, T., Yılmaz, A., 2017. East Anatolian Plateau constructed over a continental basement: no evidence for the East Anatolian Accretionary complex. Geology 45, 791–794.
- Topuz, G., Candan, O., Zack, T., Chen, F., Li, Q.-L., 2019. Early Miocene high-potassium Itype granite plutonism in the East Anatolian plateau (the Taşlıçay intrusion). Lithos 348, 105210
- Topuz, G., Candan, O., Okay, A.I., von Quadt, A., Othman, M., Zack, T., Wang, J., 2020. Silurian anorogenic basic and acidic magmatism in Northwest Turkey: implications for the opening of the Paleo-Tethys. Lithos 356, 105302.
- Turner, S.P., Foden, J.D., Morrison, R.S., 1992. Derivation of some A-type magmas by fractionation of basaltic magma: an example from the Padthaway Ridge, South Australia. Lithos 28. 151–179.
- Ustaömer, P.A., Ustaömer, T., Robertson, A.H.F., 2012b. lon probe U-Pb dating of the Central Sakarya basement: a peri-Gondwana terrane intruded by late lower Carboniferous subduction/collision-related granitic rocks. Turk. J. Earth Sci. 21, 905–932.
- Ustaömer, T., Robertson, A.H.F., Ustaömer, P.A., Gerdes, A., Peytcheva, I., 2012a. Constraints on Variscan and Cimmerian magmatism and metamorphism in the Pontides (Yusufeli–Artvin area), NE Turkey from U–Pb dating and granite geochemistry. Geol. Soc. Lond. Spec. Publ. 372, 49–74.
- Ustaomer, T., Ustaömer, P.A., Robertson, A.H., Gerdes, A., 2019. U-Pb-Hf isotopic data from detrital zircons in late Carboniferous and mid-late Triassic sandstones, and also Carboniferous granites from the Tauride and Anatolide continental units in S Turkey: implications for Tethyan palaeogeography. Int. Geol. Rev. https://doi.org/10.1080/00206814.2019.1636415.
- Uzunçimen, S., Tekin, U.K., Bedi, Y., Perincek, D., Varol, E., Soycan, H., 2011. Discovery of the late Triassic (Middle Carnian–Rhaetian) radiolarians in the volcanosedimentary sequences of the Kocali complex, SE Turkey: correlation with the other Tauride units. J. Asian Earth Sci. 40, 180–200.
- Valley, J.W., Chiarenzelli, J.R., McLelland, J.M., 1994. Oxygen isotope geochemistry of zircon. Earth Planet. Sci. Lett. 126, 187–206.
- Vesali, Y., Esmaeily, D., Moazzen, M., Chiaradia, M., Morishita, T., Soda, Y., Sheibi, M., 2020. The Paleozoic Jalal Abad mafic complex (Central Iran): implication for the petrogenesis. Geochemistry 125597.
- Watson, E.B., Harrison, T.M., 1983. Zircon saturation revisited: temperature and compositional effects in a variety of crustal magma types. Earth Planet. Sci. Lett. 64, 295–304.
- Whalen, J.B., Currie, K.L., Chappell, B.W., 1987. A-type granites: geochemical characteristics, discrimination and petrogenesis. Contrib. Mineral. Petrol. 95, 407–419.
- Winchester, J.A., the PACE TMR Network Team (contract ERBFMRXCT97-0136), 2002. Palaeozoic amalgamation of Central Europe: new results from recent geological and geophysical investigations. Tectonophysics 360, 5–21.
- Yılmaz, A., Yılmaz, H., 2019. Structural evolution of the Eastern Anatolian Basins: an example from collisional to postcollisional tectonic processes, Turkey. Turk. J. Earth Sci. 28, 329–350.
- Yılmaz, A., Terlemez, İ., Uysal, Ş., 1988. Hınıs (Erzurum GD'su) dolaylarının bazı stratigrafik ve tektonik özellikleri. Maden Tetkik ve Arama Genel Müdürlüğü Dergisi 108, 38–56.
- Yılmaz, A., Yılmaz, H., Kaya, C., Boztuğ, D., 2010. The nature of the crustal structure of the Eastern Anatolian Plateau, Turkey. Geodin. Acta 23, 167–183.